

The influence of accretion geometry on the spectral evolution during thermonuclear (type-I) X-ray bursts

Jari J. E. Kajava,^{1,2,3*} Joonas Nättilä,^{3,4} Outi-Marja Latvala,³ Miika Pursiainen,³
Juri Poutanen,^{3,4} Valery F. Suleimanov,^{5,6} Mikhail G. Revnivtsev,⁷
Erik Kuulkers¹ and Duncan K. Galloway^{8,9,10}

¹European Space Astronomy Centre (ESA/ESAC), Science Operations Department, 28691 Villanueva de la Cañada, Madrid, Spain

²Nordic Optical Telescope, Apartado 474, 38700 Santa Cruz de La Palma, Spain

³Astronomy Division, Department of Physics, P.O.Box 3000, 90014 University of Oulu, Finland

⁴Tuorla Observatory, University of Turku, Väisäläntie 20, FIN-21500 Piikkiö, Finland

⁵Institut für Astronomie und Astrophysik, Kepler Center for Astro and Particle Physics, Universität Tübingen, Sand 1, D-72076 Tübingen, Germany

⁶Kazan (Volga region) Federal University, Kremlevskaja str., 18, Kazan 420008, Russia

⁷Space Research Institute, Russian Academy of Sciences, Profsoyuznaya 84/32, 117997 Moscow, Russia

⁸Monash Centre for Astrophysics, Monash University, Clayton, Victoria 3800, Australia

⁹School of Mathematical Sciences, Monash University, Clayton, Victoria 3800, Australia

¹⁰School of Physics, Monash University, Clayton, Victoria 3800, Australia

6 December 2024

ABSTRACT

Neutron star (NS) masses and radii can be estimated from observations of photospheric radius-expansion X-ray bursts, provided the chemical composition of the photosphere, the spectral colour-correction factors in the observed luminosity range, and the emission area during the bursts are known. By analysing 246 X-ray bursts observed by the Rossi X-ray Timing Explorer from 11 low-mass X-ray binaries, we find a dependence between the persistent spectral properties and the time evolution of the black body normalisation during the bursts. All NS atmosphere models predict that the colour-correction factor decreases in the early cooling phase when the luminosity first drops below the limiting Eddington value, leading to a characteristic pattern of variability in the measured blackbody normalisation. However, the model predictions agree with the observations for most bursts occurring in hard, low-luminosity, island spectral states, but rarely during soft, high-luminosity, banana states. The observed behaviour may be attributed to the accretion flow, which influences cooling of the NS preferentially during the soft state bursts. This result implies that only the bursts occurring in the hard, low-luminosity spectral states can be reliably used for NS mass and radius determination.

Key words: accretion, accretion discs – stars: neutron – X-rays: binaries – X-rays: bursts

1 INTRODUCTION

More than 100 low-mass X-ray binary systems (LMXB) are known to produce thermonuclear (type I) X-ray bursts (see Galloway et al. 2008).¹ These X-ray bursts are powered by unstable nuclear burning of helium and/or hydrogen into heavier elements in the neutron star (NS) ‘ocean’ (see Lewin et al. 1993; Strohmayer & Bildsten 2006, for a review). Observationally they appear as rapid X-ray flashes, where the X-ray emission increases by a factor of up to ~ 100 in a few seconds, depending on the persistent emission level. After reaching the peak, the X-ray flux typically decays back to the persistent level within a few tens of seconds. A fraction of X-ray

bursts are so energetic that the Eddington limit is reached, which causes the entire NS photosphere to expand. This expansion can be seen through time resolved X-ray spectroscopy of the X-ray burst (see e.g., Figure 1). Close to the peak flux the photospheric radius expansion (PRE) causes a characteristic decrease of the observed black body colour temperature T_{bb} with a simultaneous increase in the emission area (Hoffman et al. 1980; Grindlay et al. 1980). These PRE-bursts are a very interesting sub-class of X-ray bursts, because they can be used to constrain NS masses and radii (see e.g., Fujimoto & Taam 1986; Lewin et al. 1993; Özel et al. 2009; Suleimanov et al. 2011a) and to estimate distances to the bursters (e.g., Kuulkers et al. 2003 and references therein). Accurate mass and radius measurements provide a way to probe the properties of ultra-dense matter found in the cores of NSs through a careful comparison with NS model predictions. Thus, these measurements can

* E-mail: jkajava@sciops.esa.int

¹ See also the burster list in www.sron.nl/jeanz/bursterlist.html

be used to determine whether exotic particles, such as hyperons, pion- or kaon condensates, or even de-confined quark matter form when nucleons are compressed beyond their equilibrium nuclear densities (Lattimer & Prakash 2007; Haensel et al. 2007).

Most of the NS mass and radius measurements rely on the observation that the X-ray emission comes from the NS surface and that the spectrum can be adequately fitted with a simple thermal black body model (e.g., Galloway et al. 2008; Güver et al. 2012). This way the observed colour temperature and flux can be associated with a spherical black body radius R_{bb} (Lewin et al. 1993). Assuming the entire NS surface is burning during the X-ray burst – and that the entire NS is visible (rather than being obscured by the accretion disc) – then the black body radius is related to the NS radius R through (see Lewin et al. 1993)

$$R_{\text{bb}} = R(1+z)f_c^{-2}, \quad (1)$$

where z is the gravitational redshift and f_c is the colour-correction factor, defined as the ratio of colour temperature T_c and the effective temperature T_{eff} of the photosphere ($f_c \equiv T_c/T_{\text{eff}}$; London et al. 1986, Madej et al. 2004, Majczyna et al. 2005, Suleimanov et al. 2011b, Suleimanov et al. 2012).

The most commonly used technique to measure NS masses and radii is the so called ‘touchdown method’ (e.g., Damen et al. 1990). It relies on two key assumptions. The first assumption is that at the touchdown point – which is defined as the time t_{td} when the black body radius has a local minimum and the colour temperature has a local maximum (see Figure 1) – the luminosity is at the Eddington limit, L_{Edd} , such that

$$L_{\text{td}} = L_{\text{Edd}} \equiv \frac{4\pi GMc}{\kappa} (1+z)^{-1}, \quad (2)$$

where G is the gravitational constant, M is the NS mass, c is the light speed and κ is the opacity. The second assumption is that the emission area is constant throughout the cooling and that the photospheric colour-correction factor f_c asymptotically reaches a constant value of $f_c \approx 1.4$ (see e.g., Özel et al. 2009), which is taken from NS atmosphere model predictions by Madej et al. (2004) and Majczyna et al. (2005).

However, recent NS atmosphere model calculations by Suleimanov et al. (2012) indicate that the both of these assumptions are incorrect. The Eddington luminosity can be up to 10 per cent larger as indicated by Equation (2), because of the Klein-Nishina reduction of electron scattering cross-sections from the commonly assumed Thomson value. Also, the validity of the latter assumption can be robustly checked using the existing observational data. All NS atmosphere models predict that the observer should see changes in the black body radii during the initial cooling phases of (PRE) X-ray bursts. This prediction arises from the fact that f_c should decrease when the atmosphere starts cooling and the emitted luminosity drops from the Eddington value (Madej et al. 2004; Majczyna et al. 2005; Suleimanov et al. 2011b, 2012). The most recent models of Suleimanov et al. (2012) predict that f_c is in the range 1.8–1.9 when luminosity is close to the Eddington luminosity L_{Edd} , and then f_c decreases to a range 1.4–1.5 by the time the luminosity has dropped to $0.5L_{\text{Edd}}$. Because the black body radius is proportional to the colour correction factor as $R_{\text{bb}} \propto f_c^{-2}$, we can test if X-ray burst data indeed follow the model predictions by studying the time evolution of R_{bb} during the initial first few seconds of the cooling phase.

The observed R_{bb} values are known to show variations during the cooling phases. Already in 1986, Gottwald et al. (1986) showed that R_{bb} could vary by a factor of ~ 2 in X-ray bursts

of EXO 0748–676. Similar variations were found in early observations of 4U 1636–536 by Damen et al. (1989), for 4U 1705–44 by Gottwald et al. (1989) and for 4U 1608–52 by Nakamura et al. (1989). From early on, the observed R_{bb} variations were attributed to either anisotropic emission, varying emission area, changes in the colour correction factor or a varying photospheric chemical composition (Lapidus & Sunyaev 1985; Sztajno et al. 1987; Damen et al. 1989; Lewin et al. 1993). As the R_{bb} variations are correlated with cooling time scales, they likely reflect a changing chemical composition of the NS atmosphere from burst to burst (Damen et al. 1989; Bhattacharyya et al. 2010), which can ultimately be caused by variations of the mass accretion rate \dot{M} onto the NS surface (see Fujimoto et al. 1981). Although advances have been made in recent years, it is still not clear which of these processes drive the observed R_{bb} evolution (Bhattacharyya et al. 2010; Zhang et al. 2011; Galloway & Lampe 2012; Güver et al. 2012).

In this paper, we present a new X-ray burst diagnostic to test if and when the NS cooling actually follows the atmosphere model predictions during X-ray bursts. In §2 we first describe the sample of LMXBs we have studied, and how we treated and modelled the observational data. Then in §3 we show that the NS cooling is only consistent with the models when the X-ray bursts take place during the hard, ‘island’ spectral state of the LMXBs. Because different spectral states in LMXBs are thought to be caused by variations in geometry of the inner accretion disc (see Figure 2, and Done et al. 2007 for a review), we then show in §4 that X-ray burst spectra are strongly influenced by the accretion flow in the soft, ‘banana’ spectral state, where X-ray burst cooling behaviour rarely follow the atmosphere model predictions. We therefore propose that the observed R_{bb} trends and variations in the initial cooling phases are driven by the spreading layer (SL; i.e. a boundary layer) that engulfs the NS (Inogamov & Sunyaev 1999; Popham & Sunyaev 2001; Suleimanov & Poutanen 2006; Inogamov & Sunyaev 2010). Thus, rather than observing a passively cooling NS atmosphere, we instead suggest that we are witnessing an actively accreting NS spreading layer that severely distorts the emitted X-ray burst spectra in the soft spectral states.

2 OBSERVATIONS AND DATA REDUCTION

We obtained all available *Rossi X-ray Timing Explorer* (RXTE)/PCA data from the HEASARC archive for each of the LMXBs listed in Table 1. The sample consists of two LMXB subclasses: atolls (Hasinger & van der Klis 1989) and accreting millisecond pulsars (AMP; Patruno & Watts 2012). We selected these sources, because they are known to exhibit bright X-ray bursts at a large range of persistent flux levels (Galloway et al. 2008), thus enabling us to investigate the effect of persistent accretion rate and spectral state of the LMXB on the X-ray burst emission. We did not take bright Z-sources, like Cyg X-2 (e.g., Smale 1998) or GX 17+2 (e.g., Kuulkers et al. 2002), into the sample because the high accretion rate – and consequently the elevated persistent emission level – in these systems makes it difficult to confidently determine the shape of the burst spectrum in the whole cooling track.

We identified the X-ray bursts using a similar method as in Galloway et al. (2008). Apart from finding the X-ray bursts already catalogued by them – which covered data from the beginning of the mission until June 3, 2007 – we also detected several additional X-ray bursts observed after this date. We also used similar crite-

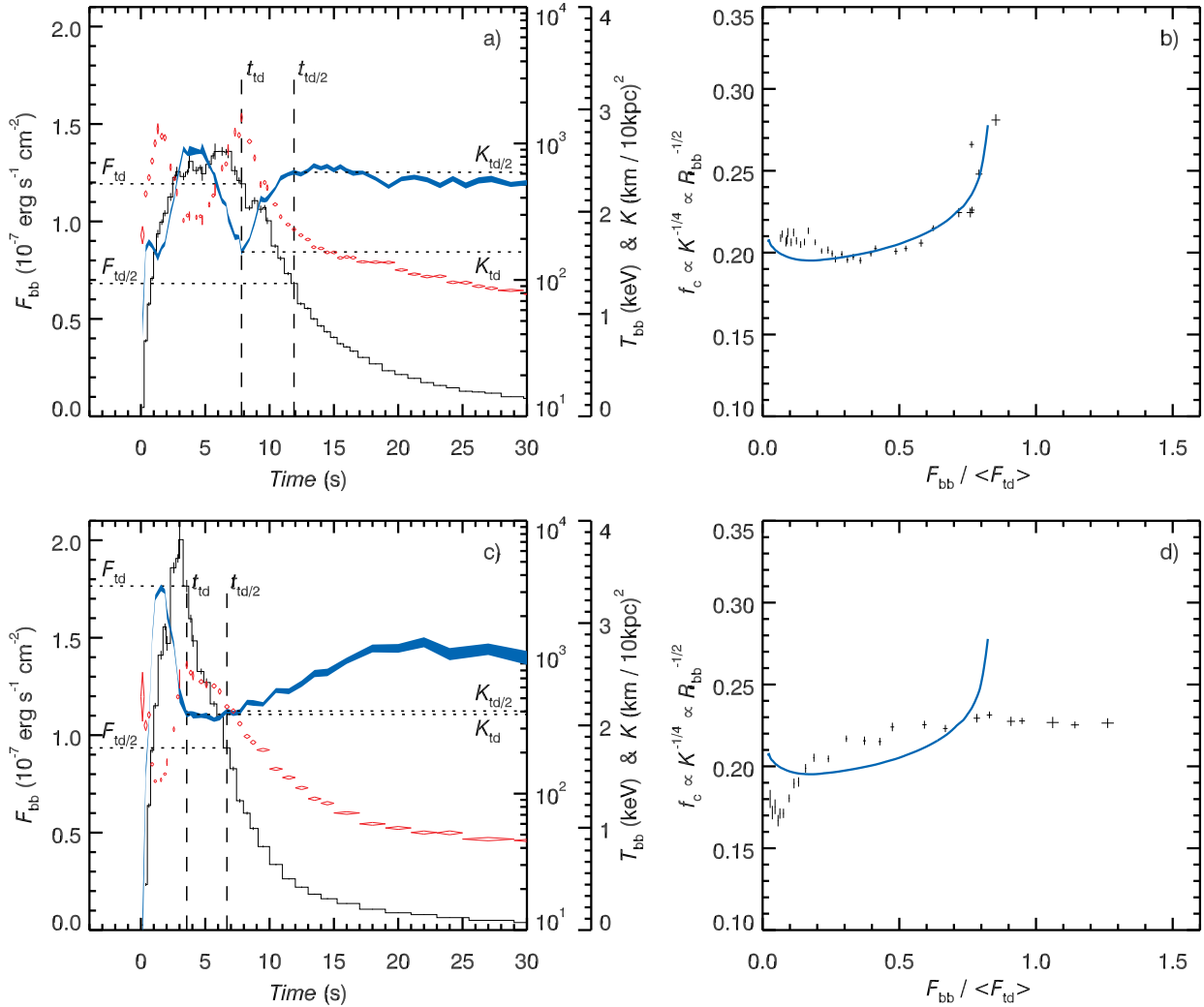


Figure 1. Time resolved spectroscopy of two PRE X-ray bursts from 4U 1608–52 illustrating the differences between hard- and soft state X-ray bursts. In panels a) and c), the black line shows the bolometric flux F_{bb} in units of $10^{-7} \text{ erg cm}^{-2} \text{ s}^{-1}$ (left-hand y-axis). The blue ribbon shows the 1σ limits of the black body normalisation $K = (R_{\text{bb}}[\text{km}]/d_{10})^2$ (inner right-hand y-axis). The red diamonds show the 1σ errors for black body temperature T_{bb} in keV (outer right-hand y-axis). The first black vertical dashed line marks the time of touchdown t_{td} and the second vertical dashed line to the right shows the time $t_{\text{td}/2}$ when F_{bb} has decreased to one half of the touchdown flux. The corresponding F_{bb} and K -values at these times F_{td} , $F_{\text{td}/2}$, K_{td} and $K_{\text{td}/2}$ are marked with dotted lines. The panels b) and d) show the relationship between the inverse square root of the black body radius (proportional to the colour-correction factor f_c) and the black body flux F_{bb} that is scaled using the mean touchdown flux $\langle F_{\text{td}} \rangle$. The blue line is a model prediction for a pure hydrogen NS atmosphere with a surface gravity of $\log g = 14.3$, taken from Suleimanov et al. (2012). The atmosphere model is the same for both b) and d) panels and it is shown here to illustrate how well (or poorly) it follows the observed data. Note that for this particular source F_{td} is strongly variable between bursts making the determination of F_{Edd} non-unique. Note also that because of telemetry issues, there are gaps in the high time resolution data around F_{td} that sometimes make touchdown time t_{td} difficult to determine.

ria as Galloway et al. (2008) to check if the X-ray burst showed signs of PRE (see Galloway et al. 2008, §2.3). If PRE was detected we included the X-ray burst to the analysis presented in this paper. However, during the analysis we had to exclude some bursts because of various technical reasons. For example, for 4U 1608–52 we excluded three bursts: one because t_{td} could not be determined due to telemetry gaps during the burst peak (OBSID: 80406-01-04-08), one because PRE was only marginal (OBSID: 70059-01-08-00) and one anomalous, marginal PRE burst where the touchdown occurs before the burst flux reaches the peak (OBSID: 94401-01-25-02). Similarly for SAX J1808.4–3658 we had to exclude the majority of the bursts that were affected by data gaps. We also did not

analyse X-ray bursts that were observed during spacecraft slews, nor the few cases where the PCA data mode was such that the determination of background and persistent emission spectra were not possible.

Altogether we analysed 246 PRE-bursts in our study (see Table A1). The *RXTE*/PCA data were reduced with the *HEASOFT* package (version 6.12) and response matrices were generated using *PCARSP* (11.7.1) task of this package. The time resolved spectra were extracted from the Event-mode data using initial integration times of 0.25, 0.5, 1.0 or 2.0 seconds, depending on the peak count rate of the burst (>6000 , 6000–3000, 3000–1500, or <1500 counts per second). Then each time the count rate after

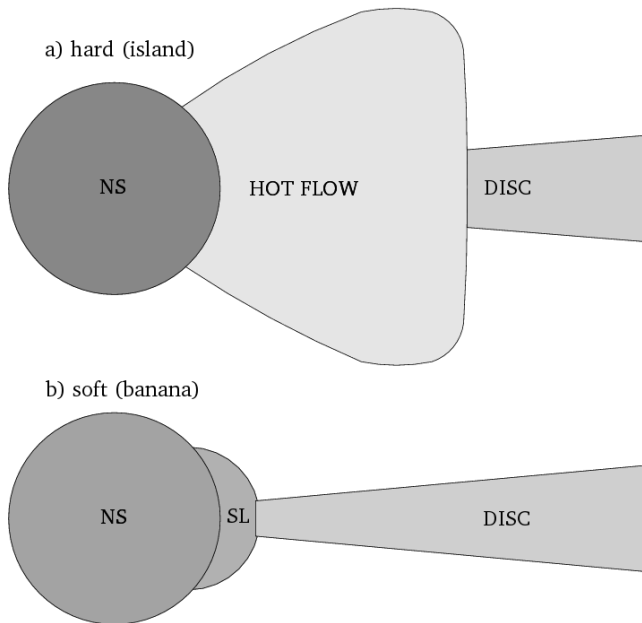


Figure 2. An illustration of the assumed accretion geometries for the LMXBs that do not show persistent pulsations. a) In the hard, island state the optically thick and geometrically thin accretion disc is assumed to be truncated at some radius, and the innermost accretion disc is assumed to form a hot, optically thin quasi-spherical flow. b) In the soft, banana state the accretion disc is assumed to reach the NS surface, where a spreading layer (SL) forms that can cover a fraction, or the entire the NS depending on the accretion rate (Inogamov & Sunyaev 1999; Suleimanov & Poutanen 2006; Inogamov & Sunyaev 2010). Note that in the soft state the accretion disc and the spreading layer also block the ‘other half’ of the NS from view, whereas in the hard state this may happen only if the truncation radius is near the NS surface and the inclination angle is large.

Table 1. The LMXBs studied in this work. The bracketed numbers in column 3 denote the number of bursts excluded from the sample. The mean touchdown flux values $\langle F_{td} \rangle$ in column 4 are given in units of $10^{-7} \text{ erg cm}^{-2} \text{ s}^{-1}$, see text. The known NS spin frequencies f_{spin} are given in Hz (see Watts 2012, table 1 and references therein).

Name	Alternative name	PRE bursts	$\langle F_{td} \rangle$	f_{spin}
4U 1608–52	4U 1608–522	18 (3)	1.40	620
4U 1636–536	V801 Ara	81 (3)	0.69	581
4U 1702–429	4U 1702–42	5 (1)	0.82	329
4U 1705–44		5 (3)	0.39	
4U 1724–307	4U 1722-30	4	0.58	
4U 1728–34	GX 354–0	79 (15)	0.95	363
4U 1735–44	V926 Sco	13	0.38	
4U 1820–30	3A 1820–303	16	0.59	
Aql X–1	V1333 Aquilae	12 (2)	1.04	550
HETE J1900.1–2455		10	1.14	377
SAX J1808.4–3658		3 (6)	2.39	401

the peak of the burst decreased by a factor of $\sqrt{2}$, the time resolution was doubled to maintain approximately the same signal-to-noise ratio. A 16 second spectrum extracted prior to the start of the X-ray burst was subtracted as the background for each burst (see Kuulkers et al. 2002; Galloway et al. 2008). We added standard 0.5 per cent systematic errors to the spectra (Jahoda et al. 2006) and paid particular attention to correct for dead-time effects by com-

puting the effective exposure time for each time bin following the approach recommended by the instrument team.² These spectra were fitted in XSPEC (Arnaud 1996) in a 2.5 – 25 keV range using Churazov-weighting (Churazov et al. 1996) because some spectral channels had very few counts. However, we note that selecting this weighting was not particularly important as we observed that results were affected only by < 1 per cent compared to the more commonly used \sqrt{N} weighting (where N is the number of counts in the detector channel). To describe the burst emission, we used a black-body model (BBODYRAD) multiplied by interstellar absorption (PHABS model in XSPEC). The best-fitting parameters were then the black body temperature T_{bb} and the normalisation constant $K_{\text{bb}} = (R_{\text{bb}}[\text{km}]/d_{10})^2$, where $d_{10} \equiv d/10\text{kpc}$ is the distance in units of 10 kpc. We initially let the absorption column density N_{H} to vary, but subsequently fixed it to the mean value over the burst. In the end, the fits using the constant mean N_{H} values were chosen for further analysis in order to minimise the number of free parameters. Different choices for the value of the absorption column densities were also studied but no significant deviations from the mean N_{H} value method was found. Errors of these parameters were taken as 1σ confidence levels, which were obtained with the ERROR task by finding $\Delta\chi^2 = 1$.

We describe the spectrum of the persistent emission through X-ray colours, which we determine using a similar approach as Done & Gierliński (2003). Instead of obtaining X-ray colours from X-ray count rates in specific *RXTE*/PCA detector channels (as is commonly done, see e.g., Galloway et al. 2008), we instead computed them from model fluxes using XSPEC. For each *RXTE*/PCA observation we divided the standard 2 data into segments of 160 seconds. We found the best fitting model using a simple procedure, where we initially started fitting the data with an absorbed POWERLAW model. We continued to add and replace model components (such as GAUSSIAN, BBODYRAD, DISKBB and COMPTT), until finding a model that could not be rejected with a higher than 95 per cent probability. In these fits we always fixed the GAUSSIAN line energy to 6.4 keV, COMPTT optical depth to $\tau = 1$, the seed photon temperature to the DISKBB temperature (when used together in the same model) and required the hydrogen column density to be within an order of magnitude of the Galactic line of sight column $N_{\text{H,gal}}$, determined using the NH ftool. We also tried to let the COMPTT seed photon temperature be a free parameter as a last resort fit, but in the majority of cases where an acceptable fit were not found before this, even this model did not provide a statistically acceptable fit. In these cases – which were approximately 3.6 per cent of all PCA spectra – we chose to ignore these spectra altogether as the colour-colour diagrams are only used for illustrative purposes. After finding the simplest best fitting model (with the smallest number of free parameters), we computed the unabsorbed fluxes using the CLUX model in XSPEC in four energy bands: 3–4 keV, 4–6.4 keV, 6.4–9.7 and 9.7–16 keV. We then defined the hard and soft X-ray colours as flux ratios of $(9.7 - 16)/(6.4 - 9.7)$ keV and $(4 - 6.4)/(3 - 4)$ keV, respectively. We also computed the persistent flux F_{per} from the same best fitting model over the 2.5–25 keV band. This method of computing the X-ray colours has the distinct advantage that it helps to mitigate the effect of interstellar absorption that causes differences the values of the soft colour in different LMXB systems. Also, this method eliminates small errors in X-ray colours due to PCA gain change related variations in energy-to-channel conversions over the lifetime of *RXTE*.

² http://heasarc.gsfc.nasa.gov/docs/xte/recipes/pca_deadtime.html

3 X-RAY BURSTS DURING DIFFERENT SPECTRAL STATES

3.1 X-ray bursts and colour-colour diagrams

Colour-colour diagrams (CC-diagrams hereafter) provide a model independent way to describe spectral evolution of LMXBs. Together with fast variability properties, the CC-diagrams provide the basis for classifying LMXBs into atoll sources and Z-sources (Hasinger & van der Klis 1989). AMPs are typically put into the atoll category (van Straaten et al. 2005), but they are different from normal atolls as they show persistent pulsations and their CC-diagrams are also distinct. In our sample, we only have atoll sources as they tend to show X-ray bursts in a large range of luminosities. The two intermittent AMPs – HETE J1900.1–2455 (Galloway et al. 2007) and Aql X–1 (Casella et al. 2008) – are occasionally seen as AMPs, but otherwise behave like normal atolls.

The CC-diagrams for the sources in our sample are shown in Figure 3. The two distinct spectral states of atolls are easily visible in the CC-diagrams. The hard spectral state (top of the CC-diagram) is called the ‘island state’, whereas the soft state is called the ‘banana branch’ (Hasinger & van der Klis 1989). As in black hole transients, the hard states tend to be seen when luminosities are low (hence at lower inferred mass accretion rates) and soft states are seen at higher luminosities (see right panels of Figure 3, and Done et al. 2007 for a review). For each source, the x-axis in the right hand panels of Figure 3 denotes the persistent flux F_{per} , which is divided by the mean flux of all bursts of a given source at the touchdown point $\langle F_{\text{td}} \rangle$. As $\langle F_{\text{td}} \rangle$ is close to the Eddington flux F_{Edd} , the ratio is approximately $F_{\text{per}}/\langle F_{\text{td}} \rangle \approx F_{\text{per}}/F_{\text{Edd}}$ and it can be used as a proxy of the mass accretion rate \dot{M} .³ However, we note that there are a few sources in our sample where $\langle F_{\text{td}} \rangle$ shows large scatter (see Fig. 1 and Table A1), so the estimate of $\langle F_{\text{td}} \rangle$ can suffer from up to ~ 30 per cent systematic inaccuracy (see also Galloway et al. 2008 for discussion). In addition, F_{per} is also computed only in limited 2.5–25 keV band. In the soft states, when the emission can be often modelled with two black-body like components, most of the flux is emitted in this band, but in hard states F_{per} can underestimate the bolometric flux by up to a factor of two (Galloway et al. 2008). Because these large systematics dominate the error budget, we do not display error bars and note that the uncertainty in the $F_{\text{per}}/\langle F_{\text{td}} \rangle$ values can be up to factor of two in the hard state.

The X-ray colours that were observed right before the X-ray burst are highlighted with coloured symbols. We used the bottom left area of the CC-diagram as the dividing line below which bursts are referred as soft state X-ray bursts. These bursts are displayed with red diagonal crosses. The hard state bursts at the top of the CC-diagram are denoted with green crosses and the ‘intermediate’ state bursts that lie in between these two well defined states are shown with blue asterisks. In a few sources, like 4U 1608–52, 4U 1636–536 and 4U 1728–34, the boundary between the soft and the intermediate bursts is not straight forward to define. In addition, for 4U 1728–34 the boundary between the hard and the intermediate bursts is not well defined either. In these sources the dividing lines were chosen somewhat arbitrarily, but the results, or the conclusions are not affected if a few bursts are moved from one category to the other.

One striking feature seen in Figure 3 is the diversity of bursting behaviour among the sources in the sample. Different sources show PRE-bursts in different regions of the CC-diagrams, and there are various reasons causing the diversity. According to the standard burst theory (Fujimoto et al. 1981; Strohmayer & Bildsten 2006), steady nuclear burning of hydrogen is thought to produce PRE-bursts in a pure helium layer in the range of $F_{\text{per}}/\langle F_{\text{td}} \rangle \sim 0.01 - 0.05$, whereas for bursts above $F_{\text{per}}/\langle F_{\text{td}} \rangle \gtrsim 0.05$ fresh accreted hydrogen builds up faster than it can burn to helium, resulting in mixed hydrogen/helium bursts. However, these dividing lines can vary from source to source for several reasons. Because the relative amount of hydrogen and helium influences the burst energetics, one of the main factors causing the diversity of bursting properties is the difference in chemical composition of the accreted fuel between sources. There are two ultra-compact binaries which accrete hydrogen poor gas: 4U 1820–30 (a white dwarf–neutron star binary with an 11-minute period, Stella et al. 1987) and 4U 1728–34 (a candidate ultra-compact binary with a possible ~ 10 minute orbital period, Galloway et al. 2010), which sets them apart from the rest of the sources in the sample. Also, as noted by Muno et al. (2004), another key effect seems to be the NS spin frequency: the ‘slowly’ spinning systems such as 4U 1702–429 and 4U 1728–34 show PRE burst only (or preferentially) in the hard states, whereas faster spinning sources such as 4U 1636–536 and Aql X–1 show PRE bursts preferentially in the soft states (see also Galloway et al. 2008). The role of turbulent mixing in the burning layers might be important to explain these differences. According to Piro & Bildsten (2007), the mixing – which is more effective at higher accretion rates and at smaller NS spin frequencies – can cause helium to burn in steady state, and thus cause the bursting to stop in different parts of the diagrams. These factors might be related to each other, because all the slow-spinning sources for which the composition is known are hydrogen-poor, while all the fast-spinning sources are hydrogen-rich (Galloway et al. 2008). However, a detailed comparison is challenging because we do not know the spin- nor orbital periods for all of the systems in the sample. Furthermore, the sources make spectral state transitions in the same \dot{M} range where the bursting regimes are expected to change. This may affect the bursting properties if the accretion geometry changes as illustrated in Figure 2. The local mass accretion rate (i.e. \dot{M} per unit NS surface area), which is important in defining the bursting properties, might change in an opposite way during the transitions as indicated by the global \dot{M} (see, e.g., Bildsten 2000). In addition, the presence of dynamically important magnetic fields in the AMP SAX J1808.4–3658 – and to some extent in the intermittent AMPs (Aql X–1 and HETE J1900.1–2455) – influences the accretion geometry, which further complicates the comparison of the bursting behaviour between the sources in the sample.

Although the bursting behaviour is diverse and not necessarily fully understood yet, we can nevertheless investigate how the evolution of the black body normalisation (and thus R_{bb}) depends on the spectral state the burst occurred, given that a large number of PRE-bursts are detected in different spectral states between the sources in the sample.

3.2 A new X-ray burst diagnostic: the K-ratio

Because of the large collecting area of *RXTE*/PCA and the brightness of the sources in the sample, we can perform time-resolved spectroscopy of the bursts in the initial cooling phases. The most recent models of Suleimanov et al. (2012) predict that the colour correction factor f_c should drop from 1.8–1.9 at touchdown to 1.4–

³ Note that this ratio is similar to the commonly used \dot{M} -proxy $\gamma \equiv F_{\text{per}}/\langle F_{\text{peak}} \rangle$, where $\langle F_{\text{peak}} \rangle$ is the mean peak flux (van Paradijs et al. 1988; Galloway et al. 2008).

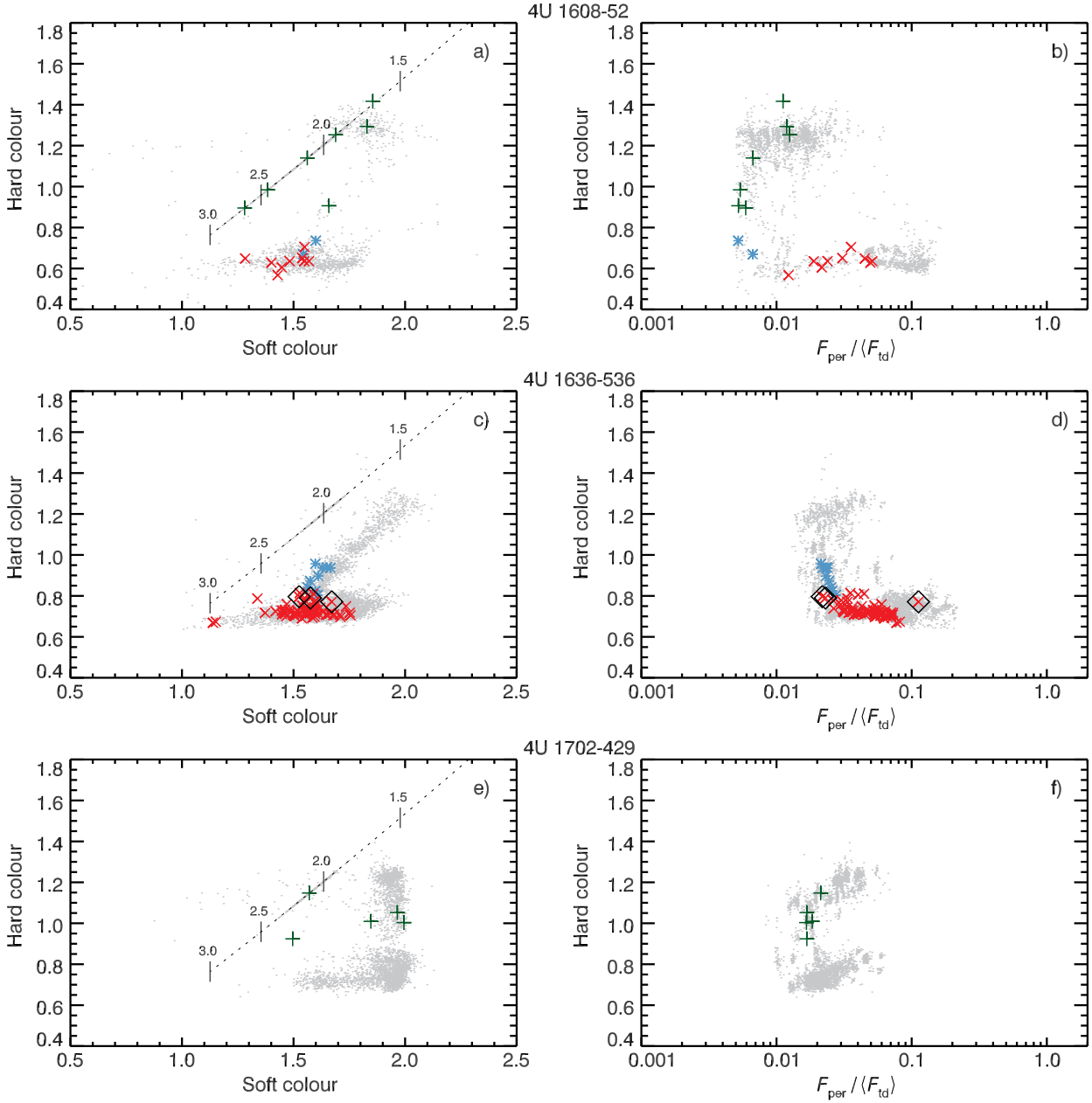


Figure 3. Left panels: colour-colour (CC) diagrams for each LMXB in the studied sample. The dotted line indicates the track for spectra consisting of an absorbed power-law, with the spectral index Γ indicated. The hard- and the soft X-ray colours are flux ratios between $(9.7 - 16)/(6.4 - 9.7)$ keV and $(4 - 6.4)/(3 - 4)$ keV, respectively. The colours for the 160 second segments just before the PRE bursts are highlighted with green crosses, red diagonal crosses and blue asterisks for PRE bursts in hard, soft and ‘intermediate’ states, respectively (the rest are marked with grey dots). Right panels have the same y-axes as left panels, but the x-axes show the persistent flux F_{per} scaled with the mean touchdown flux $\langle F_{\text{td}} \rangle$. Three bursts of 4U 1636–536 are highlighted using diagonal boxes for easier cross-referencing with Figure 4.

1.5 before the flux had dropped to half of it. According to Equation (1) the black body normalisation $K \propto R_{\text{bb}}^2 \propto f_c^{-4}$ and, therefore, to see when bursts follow this expected behaviour, we devised a very simple diagnostic. We extracted two black body flux and normalisation values from the data for each X-ray burst (see Figure 1). We first located the touchdown time t_{td} , and the corresponding flux and black body normalisation at touchdown $F_{\text{td}}(t = t_{\text{td}})$ and $K_{\text{td}}(t = t_{\text{td}})$. We then located the same values after the flux had dropped to half of the touchdown flux, i.e. $F_{\text{td}/2}(t = t_{\text{td}/2})$ and $K_{\text{td}/2}(t = t_{\text{td}/2})$, where $F_{\text{td}/2}(t = t_{\text{td}/2}) = 0.5F_{\text{td}}(t = t_{\text{td}})$ (we

took the values just before flux dropped below $0.5F_{\text{td}}$). We then took a ratio of these normalisation values $K_{\text{td}/2}/K_{\text{td}} \propto (R_{\text{bb}}(t = t_{\text{td}/2})/R_{\text{bb}}(t = t_{\text{td}}))^2 \propto (f_c(t = t_{\text{td}/2})/f_c(t = t_{\text{td}}))^{-4}$ because this ratio does not depend on the distance, nor the unknown gravitational redshift. We then plot the $K_{\text{td}/2}/K_{\text{td}}$ ratios of all the bursts in the sample as a function of the scaled persistent flux $F_{\text{per}}/\langle F_{\text{td}} \rangle$ in Figure 4. We use the same colour coding as in the CC-diagrams of Figure 3. In Figure 4 we also show the area where $K_{\text{td}/2}/K_{\text{td}} \propto (f_c(t = t_{\text{td}/2})/f_c(t = t_{\text{td}}))^{-4}$ ratios are consistent with Suleimanov et al. (2012) model predictions. Even if we

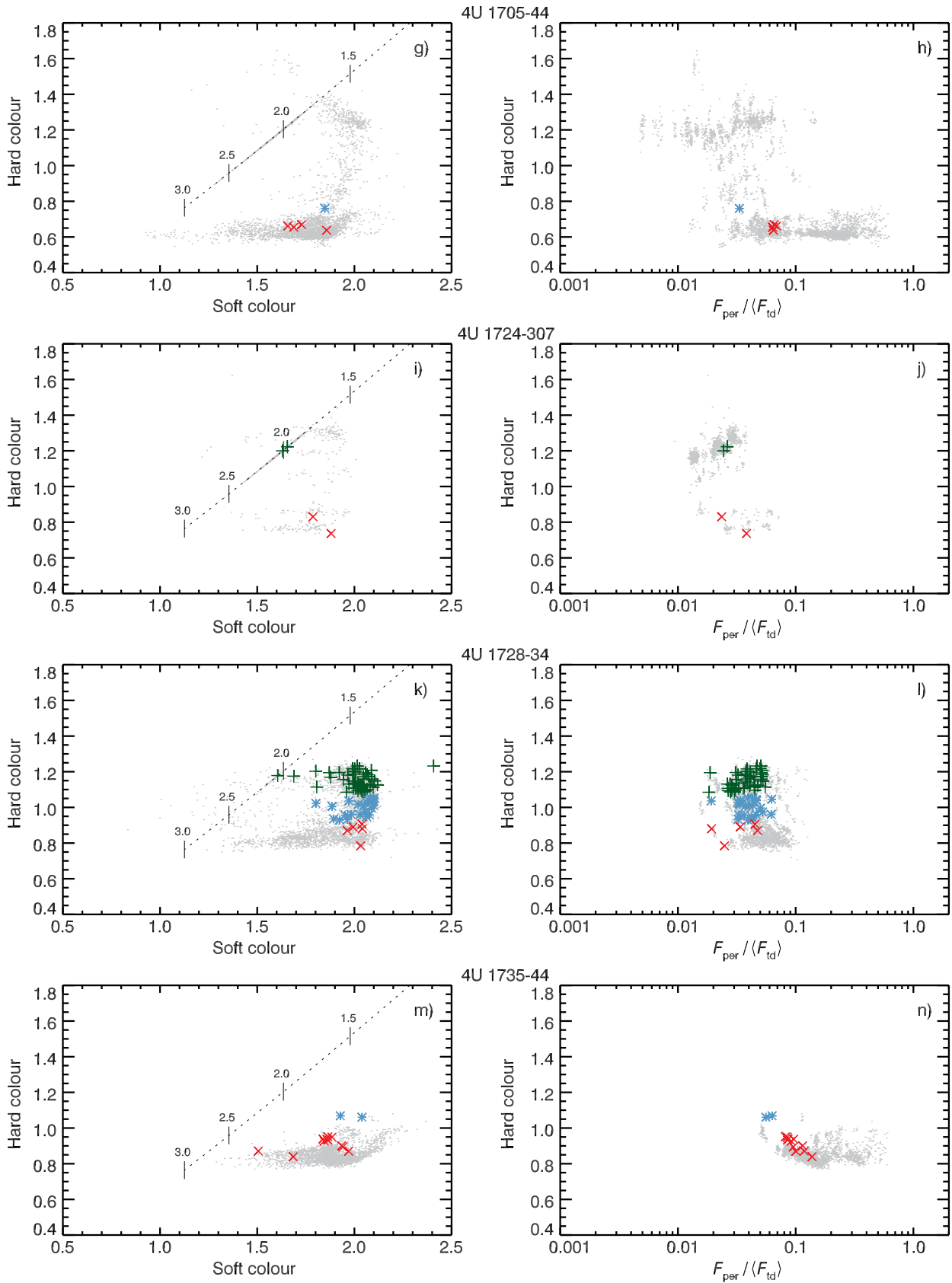


Figure 3 – continued

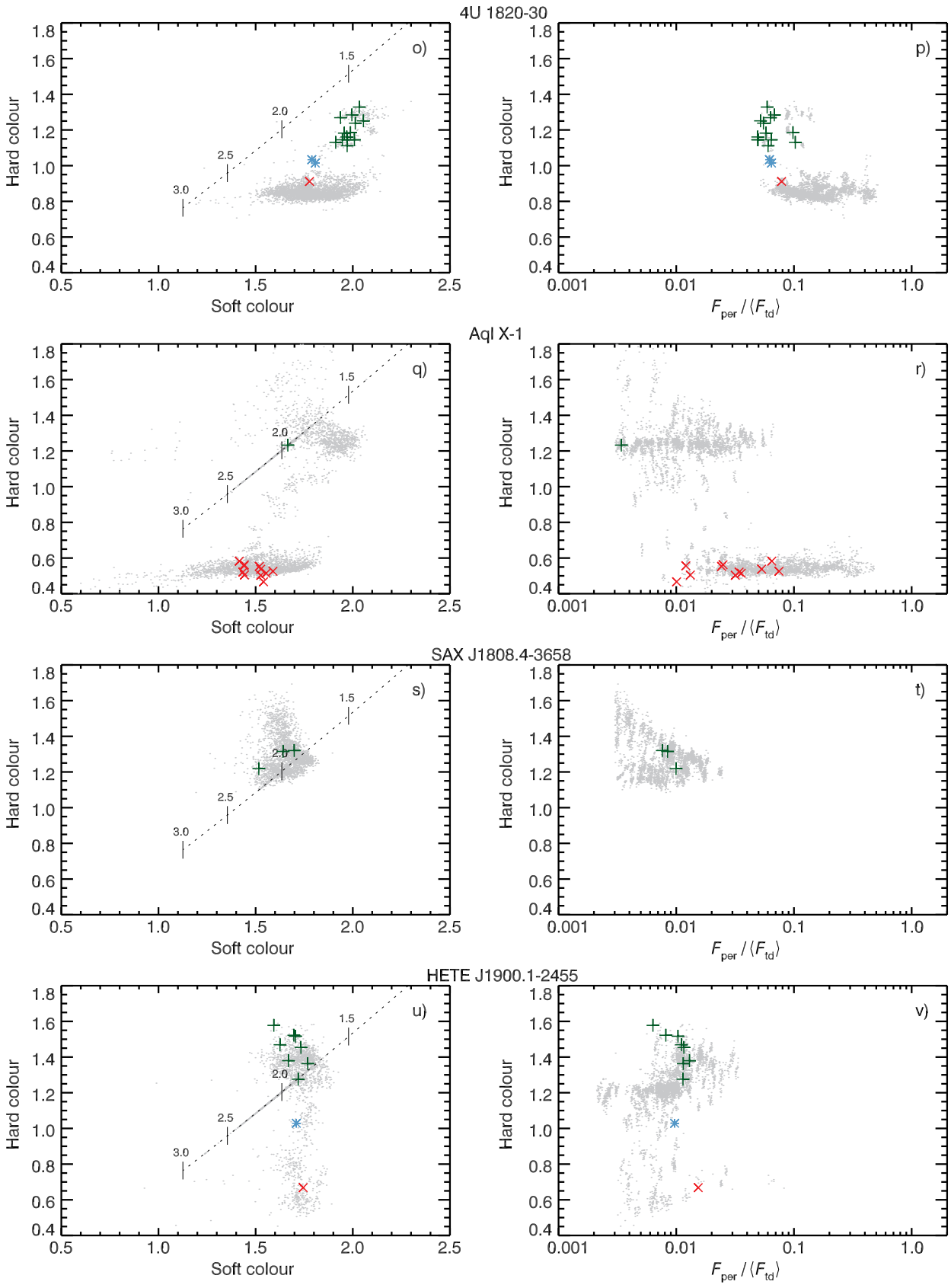


Figure 3 – continued

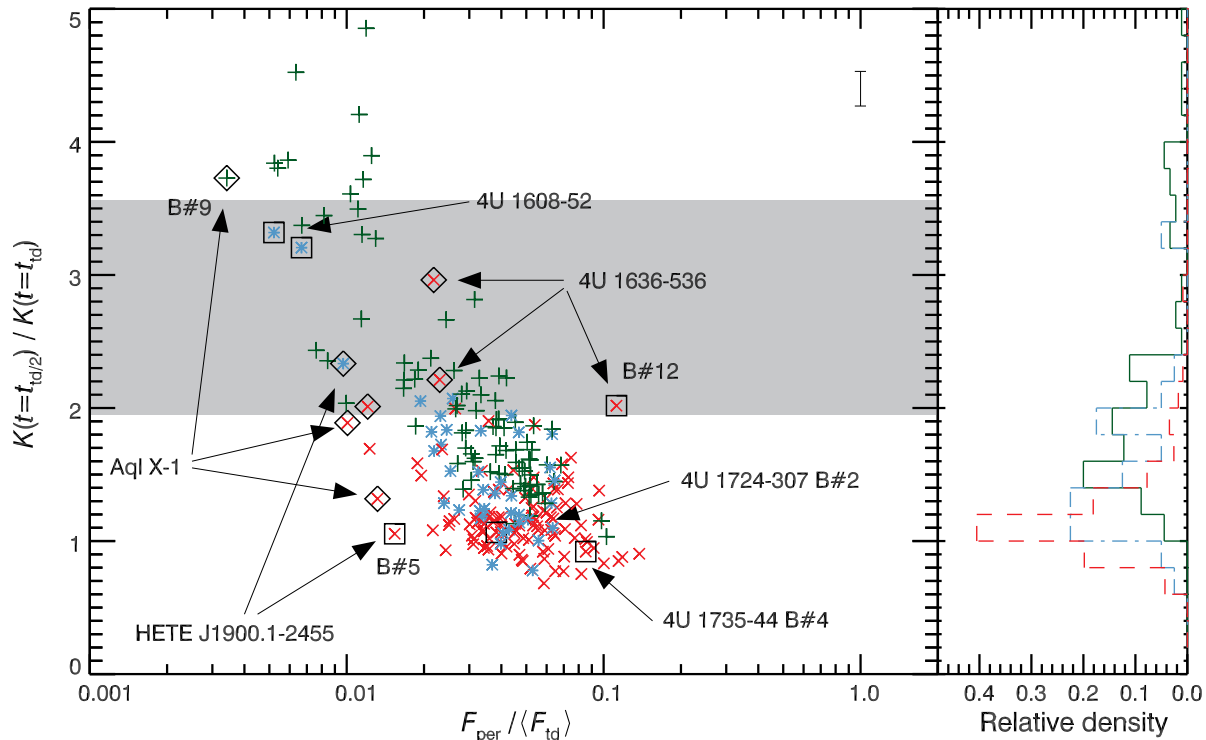


Figure 4. Ratio of black body normalisations at ‘half-touchdown’ and at touchdown as a function of the scaled persistent flux $F_{\text{per}}/\langle F_{\text{td}} \rangle$. The symbol colours are based on the CC-diagrams (left panels of Figure 3) with green crosses, red diagonal crosses and blue asterisks denoting PRE bursts that occur during hard, soft and ‘intermediate’ states, respectively. Note also that the x-axis is the same as in the right hand side panels of Figure 3 and that the way how K -values in the y-axis are computed is illustrated in Figure 1. The grey horizontal band denotes the area where $K_{\text{td}/2}/K_{\text{td}} \propto (f_c(t = t_{\text{td}/2})/f_c(t = t_{\text{td}}))^{-4}$ ratio is consistent with Suleimanov et al. (2012) models predictions (see text). The right panel histograms show how bursts in different spectral states are distributed differently on this diagram (hard, soft and ‘intermediate’ state histograms are marked with a green line, a red dashed line and a blue dash-dotted line, respectively). Only the hard state bursts that take place at persistent fluxes lower than ~ 3 per cent of the Eddington value are consistent with the model predictions. Those hard state bursts that have $K_{\text{td}/2}/K_{\text{td}} < 2$ are all from two sources: 4U 1728–34 and 4U 1820–30. A few interesting bursts that have significantly lower touchdown fluxes than $\langle F_{\text{td}} \rangle$ are highlighted with squares, whereas other interesting ‘outlier’ bursts (with $F_{\text{td}} \gtrsim \langle F_{\text{td}} \rangle$) are highlighted using diagonal boxes (see discussion in Section 4.3).

allow the NS photosphere to change composition during the burst, the K -ratios should be in a tight range between $\approx 2.0 - 3.6$.

The PRE bursts that occur during hard- and soft states have clearly different $K_{\text{td}/2}/K_{\text{td}}$ ratios. We can rule out the possibility that the X-ray burst cooling tracks in these two states come from the same underlying distribution, because the chi-squared test on the hard- and soft state $K_{\text{td}/2}/K_{\text{td}}$ histograms gives $\chi^2 = 66.14$ for 19 degrees of freedom (p – value $\approx 4 \times 10^{-7}$; alternatively the value of Kolmogorov-Smirnov D -statistic is $D = 0.705$ and p – value $< 10^{-8}$; see Press et al. 2007). The majority of soft state bursts have $K_{\text{td}/2}/K_{\text{td}} \approx 1$, and only 4 out of 116 of them have $K_{\text{td}/2}/K_{\text{td}} > 2$.

In contrast, about 40 per cent of hard state bursts have $K_{\text{td}/2}/K_{\text{td}} > 2$ and all the hard state bursts that do not follow the model predictions, i.e. that have $K_{\text{td}/2}/K_{\text{td}} < 2$, are from the two ultra-compact sources: 4U 1728–34 and 4U 1820–30. In these two cases at very close to Eddington flux there is a characteristic kink upwards in the $F - K^{-1/4}$ diagrams, similar to the burst shown in Figure 1 b), but the behaviour later on is not consistent with model predictions (see also García et al. 2013, figure 6). However, it is not clear why the hard state K -ratios in these hydrogen poor systems are so different from the rest of the sample. The results in Figure 4 nevertheless show that only bursts that occur during the hard state,

and occur below ~ 3 per cent of the Eddington luminosity are consistent with the model predictions.

4 DISCUSSION

4.1 Effects of the accretion flow

If none of the X-ray bursts followed the NS atmospheric model predictions of Suleimanov et al. (2012), then we would have a strong reason to doubt that some essential piece of physics is still missing from the models (like stellar rotation). However, the results presented in Figure 4 show that this is not the case. We can see that there are a large number of X-ray bursts that fall within the band where they are consistent with the atmosphere models: most of them being bursts that occur during low-luminosity, hard states. Therefore one should rather be asking why, apart from a few outliers, the X-ray bursts in the soft state do not follow the expected cooling behaviour.

The data clearly indicates that the emission area for the soft state bursts remain approximately constant, that is, the K -ratio is $K_{\text{td}/2}/K_{\text{td}} \approx 1$. This can only be realised if the emitting area and the colour correction factor stay constant during the initial cooling phase (Galloway & Lampe 2012). An interpretation of this be-

behaviour was given in Suleimanov et al. (2011a), where PRE-bursts of 4U 1724–307 were analysed. This interpretation assumes that the two spectral states are caused by changes in the accretion geometry, which is illustrated in Figure 2. The origin of the constant black body radius could be related to the spreading layer (SL, Inogamov & Sunyaev 1999, 2010), but we emphasise that the key point is not the emission produced by the SL itself; it can be determined from the spectrum of the persistent emission moments before the burst and it can be subtracted from the burst emission (as is routinely done in X-ray burst analysis). Rather, the SL changes the X-ray burst radiation spectrum, because the emission from the X-ray burst must pass through this layer before reaching the observer. As the accreted gas enters the SL with roughly Keplerian orbital frequency (always larger than the NS spin frequency), the SL is supported both by centrifugal forces and the radiation pressure force produced by energy dissipation within the SL and by the X-ray burst. This makes the outermost layers of the SL tenuous and, therefore, the resulting radiation spectrum has colour correction factor of about $f_c \approx 1.6 - 1.8$ for a large range of luminosities from $L \sim L_{\text{Edd}}$ to $L \sim 0.2L_{\text{Edd}}$ (Suleimanov & Poutanen 2006; Revnivtsev et al. 2013). In our view, this can explain the irregular cooling behaviour of X-ray bursts in the soft state where the black body radius R_{bb} is constant in the aforementioned luminosity range (i.e. $K_{\text{td}/2}/K_{\text{td}} \approx 1$). However, the constancy of R_{bb} in the soft state bursts does not mean that we see the entire NS surface, as is commonly proposed (e.g., Lattimer & Steiner 2014). The R_{bb} can also be constant in the soft state bursts if the SL always blocks a constant fraction (about the half) of the NS from view.

In addition, we speculate that the SL causes also another observable feature in the time evolution of R_{bb} values in the late cooling stages when $L \lesssim 0.5L_{\text{Edd}}$ (see Figure 1d). According to Inogamov & Sunyaev (1999, 2010), the latitudinal width of the SL depends on the accretion rate and thus the luminosity. However, when an X-ray burst occurs beneath the SL it provides additional radiation support to this levitating layer. When the NS atmosphere starts cooling immediately after the X-ray burst peak and the luminosity starts decaying from the Eddington value, the SL above the NS starts to be less and less supported by the radiation pressure produced by the burst. During the first moments after the X-ray burst, when the luminosity is close to the Eddington value, the SL might cover the whole NS (see Inogamov & Sunyaev 1999, figure 7). Over the next few seconds, when the burst luminosity drops towards the level of the persistent emission, the SL may instead cover a smaller fraction of the NS surface. The polar regions of the NS would then be gradually exposed to the observer as the luminosity drops. This polar region would have $f_c \approx 1.4$, whereas the equatorial regions of the star would still be covered beneath the SL with $f_c \approx 1.6 - 1.8$. Such uncovering of the NS surface would have the net effect of gradually decreasing the colour correction factor when the burst luminosity drops. We speculate that this might cause the observed R_{bb} variations below $\sim 0.2 F_{\text{Edd}}$ in the burst presented in Figure 1(d) (see also Poutanen et al. 2014). Similar behaviour is seen in the late stages of soft state bursts (and the non-PRE hard state bursts) of 4U 1636–536 (see figure 7 in Zhang et al. 2011). Future theoretical research towards this direction would be of interest, because if our interpretation is correct in a qualitative sense, then, in principle, these soft state X-ray burst could be used to place constraints on how the latitudinal width of spreading layers depend on the luminosity.

4.2 Implications for NS mass and radius measurements

The most profound implication of our result has to do with the NS mass and radius constraints that can be derived from the PRE-bursts. Apart from rare exceptions (such as the analysis presented in van Paradijs et al. 1990), there are many examples in the literature where soft state X-ray bursts have been used to make NS mass-radius estimates (see e.g., Fujimoto & Taam 1986; Sztajno et al. 1987; Özel et al. 2009; Güver et al. 2010a; Güver & Özel 2013). In addition the hard state bursts of 4U 1820–30, which occur above the ~ 3 per cent of Eddington threshold, have been used to make mass-radius constraints (van Paradijs & Lewin 1987; Güver et al. 2010b). However, in both cases the data are not consistent with the NS atmosphere model predictions (see also the critical discussion in García et al. 2013). There are various studies about the NS equation of state that are at least partly based on these measurements (e.g., Steiner et al. 2010; Özel et al. 2010; Lattimer & Steiner 2014), which in light of the results presented here need to be revisited. The reason for this statement is simple and holds even if our interpretation of the R_{bb} evolution in soft state bursts is incorrect; it can be seen in the two bursts of 4U 1608–52 shown in Figure 1(b) and (d). Clearly, the hard state burst (panel b) is consistent with the atmosphere model predictions, whereas the soft state burst (panel d) is not. The results presented in Figure 4 also argue that the soft state bursts are not consistent with NS atmosphere models. Previous NS mass-radius constraints are typically obtained from the soft state bursts, using the NS atmosphere models by taking $f_c \approx 1.4$ in the cooling tail, even if the predictions are not consistent with the data closer to Eddington luminosity. In addition, the hard state bursts are typically excluded from the analysis using ad hoc arguments. This is clearly inconsistent and these ‘selection effects’ – and their impact on the NS mass-radius estimates – are further highlighted for 4U 1608–52 in Poutanen et al. (2014).

One clear conclusion comes out of the results presented in this paper. In order to make self-consistent NS mass-radius constraints using PRE-bursts, one must choose only the hard state bursts that occur at persistent flux levels below ~ 3 per cent of Eddington. However, further improvements into the NS atmosphere models are needed before accurate mass-radius constraints can be obtained. The stellar rotation is not yet incorporated to the Suleimanov et al. (2012) models, but these models are being computed (Suleimanov et al., in prep.) and they will be applied to the hard state bursts presented in this study (these results will be presented in Nättälä et al., in prep.).

4.3 Open issues

There are still many unanswered issues in the rich *RXTE*/PCA data set regarding the behaviour of the bursters. The hard state bursts in the ultra-compact systems, 4U 1728–34 and 4U 1820–30, seem to behave differently with respect to the bursts from the rest of the atoll sources in the sample; the origin for this is not understood at present. It would be interesting to investigate if the behaviour of other ultra-compact systems (see e.g., in’t Zand et al. 2007) are also different from the atolls with longer orbital periods. However, the K-ratios cannot be easily computed for most of the candidate systems because they either do not show PRE-bursts or the bursts are too faint to resolve the cooling track from F_{td} to $F_{\text{td}/2}$. A careful comparison with the Z-sources might also be useful. For example, the soft state bursts of GX 17+2 follow the canonical $L \propto T^4$ track, which implies K-ratios of $K_{\text{td}/2}/K_{\text{td}} \approx 1$ (see e.g., Kuulkers et al.

2002, figure 13), but, as discussed in Section 2, the intense persistent emission complicates the analysis substantially.

In Figure 4 one can also see various hard state bursts with high K-ratios of $K_{td/2}/K_{td} \gtrsim 3.6$. These bursts tend to also be the longest and the most energetic ones. One of the systems showing these bursts is 4U 1608–52 and, as in Poutanen et al. (2014), we speculate that in these bursts the nuclear burning ashes might have reached the photosphere (Weinberg et al. 2006), leading to a lower f_c at around half Eddington luminosity, and thus higher K-ratio.

In addition, from Figure 4 it is evident that there are a few interesting ‘non-hard-state’ bursts that have K-ratios consistent with the Suleimanov et al. (2012) models. Especially the burst #12 from 4U 1636–536 that is highlighted in Figure 4 seems to be a clear outlier. The touchdown flux of $F_{td} = (0.409 \pm 0.009) \times 10^{-7} \text{ erg cm}^{-2} \text{ s}^{-1}$ for this particular burst is clearly below the mean of 4U 1636–536 $\langle F_{td} \rangle = 0.69 \times 10^{-7} \text{ erg cm}^{-2} \text{ s}^{-1}$. It was argued by Galloway et al. (2006) that for this faint PRE burst, the Eddington limit for hydrogen-rich atmosphere was reached, whereas the rest of the PRE bursts reach the Eddington limit for a pure helium atmosphere. However, it is not clear why the presence of the hydrogen layer in this burst causes the K-ratio to be so radically different from the rest of the soft state bursts. By comparing this faint PRE burst to the bursts from other sources in the sample that show similar bi-modality in the F_{td} values, we can see very interesting differences between the sources:

- The PRE bursts in the faint F_{td} group of 4U 1608–52 have high K-ratios, likely because they all occur in the hard state below the ~ 3 per cent of Eddington threshold.

- In contrast to 4U 1608–52, the only hard state PRE burst of Aql X–1 (burst #9) is clearly in the bright F_{td} group, but it still has a high K-ratio. On the other hand, the soft state bursts of Aql X–1 have K-ratios of the order of unity with no apparent dependence between F_{td} (nor F_{per}), indicating that the lower F_{td} value in the burst #12 from 4U 1636–536 was not the only factor leading to a high K-ratio.

- Also, the faint PRE bursts of 4U 1724–307 (burst #2) and HETE J1900.1–2455 (burst #5) both occur in the soft state and at highest F_{per} , but they have $K_{td/2}/K_{td} \approx 1.0$.

- Finally, it is also interesting to note that there is absolutely nothing remarkable in the only faint PRE burst of 4U 1735–44 (burst #4) in terms of F_{per} or its position in the CC-diagram.

The cause for these differences cannot be related to the stellar spin, because both 4U 1608–52 and Aql X–1 are fast rotators with $f_{spin} \sim 600$ Hz. Magnetic fields are likely not important either in this respect, because both Aql X–1 and HETE J1900.1–2455 are intermittent pulsars, but still show clear differences in their bursting behaviours. The persistent flux level should not affect either, because the faint PRE burst of 4U 1735–44 (burst #4) takes place at comparable \dot{M} as the burst #12 from 4U 1636–536, but, as noted above, it has $K_{td/2}/K_{td} \approx 1.0$. Perhaps the determining factor is the composition of the accreted fuel, as the ultra-compact binary 4U 1820–30 stands out again as having the stable F_{td} values. Or, alternatively, some favourable combination of these factors might occasionally cause the accretion flow to disturb the NS photosphere to a lesser extent, thus leading to K-ratios which are consistent with the Suleimanov et al. (2012) model predictions. But it must be admitted that it is very hard to draw solid conclusions of this diversity based on the limited sample of bursters we have studied.

The inner hot flow is optically thin in the low-luminosity, hard states and if the disc truncation radius is large enough, we probably always see the entire NS surface during X-ray bursts in this state.

However, the hot flow might also leave its imprint on the observed burst spectra. We have seen that some bursters show a large scatter in the absolute R_{bb} values between different hard state bursts (see also Güver et al. 2012), although they show the expected increase of R_{bb} values in the initial cooling phases. This effect is not that well visible in the K-ratios that are shown in Figure 4, because the individual X-ray bursts tend to follow the NS atmosphere model predictions and thus by taking the ratio of the two R_{bb} values, the scatter is cancelled out to some extent. This scatter is especially prominent for the two bursters showing large number of bursts: 4U 1636–536 (Zhang et al. 2011) and 4U 1728–34 (Güver et al. 2012), but similar variations are also in seen other systems, like 4U 1608–52 (Poutanen et al. 2014). It is possible that a fraction of burst photons are up-scattered by the energetic electrons in the hot flow producing a high-energy tail (and at the same time cooling the electrons) thus altering the spectrum of the persistent emission (Ji et al. 2014). This effect might cause extra spectral hardening of the burst emission and influence f_c , and if the properties of the hot flow vary from burst to burst (as seen in the CC-diagrams), then it might cause the scatter in the absolute R_{bb} values. One cannot either rule out that a small, but variable amount of nuclear burning ashes reaches the photosphere in all PRE-bursters (as in the $K_{td/2}/K_{td} \gtrsim 3.6$ bursts), leading to burst-to-burst f_c variations, which also might cause the observed R_{bb} scatter. However, these possibilities should not be as prominent sources of systematic error in the mass-radius estimates as the spreading layer in the high persistent flux, soft state bursts. Furthermore, the study by Worpel et al. (2013) indicates that the burst spectra are better described statistically if the persistent emission is allowed to vary by letting the ‘background’ model normalisation vary by a factor f_a , where high f_a values are interpreted as an increase of the mass accretion rate during the burst. However, it is not yet clear if the simple method used by Worpel et al. (2013) adequately captures the complexity of burst-disc interactions. Indeed, Peille et al. (2014) recently argued that the presence of high frequency quasi-periodic oscillations (QPO) before and during the X-ray bursts, while f_a is still above unity, is not consistent with this methodology: the high frequency QPOs are thought to be produced in the inner disc regions, but the high f_a values imply that this region would be accreted onto the NS. However, this argument breaks down if the QPOs are associated with the spreading layer as suggested by the Fourier-frequency resolved spectra (Gilfanov et al. 2003).

These are clearly important issues that should be investigated further because they might affect the NS mass-radius measurements. This means that the applicability of the new atmosphere models – and the ‘cooling tail method’ in general (Suleimanov et al. 2011a) – for all the hard state bursts is, therefore, not yet fully clear. These issues are, however, under investigation and they will be addressed in future publications.

5 SUMMARY AND CONCLUSIONS

We have presented an analysis of 246 X-ray bursts from 11 LMXB systems. Our main finding is that the evolution of the black body radii during the initial cooling phases of X-ray bursts depends on the spectral state and the accretion rate. These differences are seen in the K-ratios, i.e., in the ratio between the black body normalisation at ‘half-touchdown flux’ and at the touchdown $K_{td/2}/K_{td}$. The hard state bursts tend show a characteristic increase of the black body radius in the early cooling phase ($K_{td/2}/K_{td} > 2$), which is consistent with NS atmosphere model predictions of

Suleimanov et al. (2012). In particular, we find that only hard state bursts that have persistent fluxes below a critical threshold of about ~ 3 per cent of the Eddington value follow the NS atmosphere model predictions. Practically all soft state bursts and even hard state bursts from the candidate ultra-compact systems that take place above this critical threshold do not; they instead have $K_{\text{td}/2}/K_{\text{td}} \approx 1$, which is not consistent with any NS atmosphere model prediction.

This result supports the interpretation of Suleimanov et al. (2011a), where bursts of 4U 1724–307 were analysed; the accretion flow plays an important role in shaping the energy spectra of X-ray bursts. In the soft state the spreading layer that engulfs the NS causes the colour correction factor to have a high, constant value of about $f_c \approx 1.6 - 1.8$ over a large range of luminosities from the Eddington flux down to a fraction of it. In addition, the spreading layer can also block part of the NS surface from view in the soft state, but not necessarily in the hard state. These two effects together can explain why the black body radii are constant in the soft state bursts and why large differences are seen in the inferred NS radii between hard- and soft state bursts. The results presented here show that this behaviour is ubiquitous among atoll sources.

The effects of the accretion flow are ignored in almost all previous studies that use the soft state bursts to constrain NS masses and radii. Our results indicate that the X-ray bursts in this state are influenced by the accretion flow to such an extent that all previous NS mass-radius estimates need to be revised. This is because the two main assumptions that are used – i.e. $f_c = 1.4$ and the entire NS surface is seen – are not consistent with the data. In fact, disentangling the effects of the accretion flow from the burst emission might be so non-unique and non-trivial that the soft state bursts should not be used to constrain NS masses and radii at all. Rather, they might be better laboratories to investigate the dynamical behaviour of spreading layers.

ACKNOWLEDGEMENTS

JJEK acknowledges partial financial support from the Finnish Graduate School in Astronomy and Space Physics, the Emil Aaltonen Foundation and the Väisälä Foundation. JN also acknowledges financial support from the Väisälä Foundation. This research was supported by Academy of Finland grant 268740 (JP). VS thanks DFG (grant SFB/Transregio 7 “Gravitational Wave Astronomy”), Russian Foundation of Fundamental Research (grant 12-02-97006-r-povolzhe-a) and the COST Action MP1104 for support. DKG is the recipient of an Australian Research Council Future Fellowship (project FT0991598). We thank the International Space Science Institute (ISSI) located in Bern, Switzerland, for sponsoring an International Team on type-I X-ray bursts where early results of this project were discussed. This research made use of the NASA Astrophysics Data System and of the data obtained from the High Energy Astrophysics Science Archive (HEASARC), which is a service of the Astrophysics Science Division at NASA/GSFC and the High Energy Astrophysics Division of the Smithsonian Astrophysical Observatory.

REFERENCES

- Arnaud K. A., 1996, in Jacoby G. H., Barnes J., eds, ASP Conf. Ser. Vol. 101, *Astronomical Data Analysis Software and Systems V*. Astron. Soc. Pac., San Francisco, p. 17
- Bhattacharyya S., Miller M. C., Galloway D. K., 2010, *MNRAS*, 401, 2
- Bildsten L., 2000, in Holt S. S., Zhang W. W., eds, *AIPC*, p. 359
- Casella P., Altamirano D., Patruno A., Wijnands R., van der Klis M., 2008, *ApJ*, 674, L41
- Churazov E., Gilfanov M., Forman W., Jones C., 1996, *ApJ*, 471, 673
- Damen E., Jansen F., Penninx W., Oosterbroek T., van Paradijs J., Lewin W. H. G., 1989, *MNRAS*, 237, 523
- Damen E., Magnier E., Lewin W. H. G., Tan J., Penninx W., van Paradijs J., 1990, *A&A*, 237, 103
- Done C., Gierliński M., 2003, *MNRAS*, 342, 1041
- Done C., Gierliński M., Kubota A., 2007, *A&ARv*, 15, 1
- Fujimoto M. Y., Hanawa T., Miyaji S., 1981, *ApJ*, 247, 267
- Fujimoto M. Y., Taam R. E., 1986, *ApJ*, 305, 246
- Galloway D. K., Lampe N., 2012, *ApJ*, 747, 75
- Galloway D. K., Morgan E. H., Krauss M. I., Kaaret P., Chakrabarty D., 2007, *ApJ*, 654, L73
- Galloway D. K., Muno M. P., Hartman J. M., Psaltis D., Chakrabarty D., 2008, *ApJS*, 179, 360
- Galloway D. K., Psaltis D., Muno M. P., Chakrabarty D., 2006, *ApJ*, 639, 1033
- Galloway D. K., Yao Y., Marshall H., Misanovic Z., Weinberg N., 2010, *ApJ*, 724, 417
- García F., Zhang G., Méndez M., 2013, *MNRAS*, 429, 3266
- Gilfanov M., Revnitsev M., Molkov S., 2003, *A&A*, 410, 217
- Gottwald M., Haberl F., Langmeier A., Hasinger G., Lewin W. H. G., van Paradijs J., 1989, *ApJ*, 339, 1044
- Gottwald M., Haberl F., Parmar A. N., White N. E., 1986, *ApJ*, 308, 213
- Grindlay J. E., et al., 1980, *ApJ*, 240, L121
- Güver T., Özel F., 2013, *ApJ*, 765, L1
- Güver T., Psaltis D., Özel F., 2012, *ApJ*, 747, 76
- Güver T., Özel F., Cabrera-Lavers A., Wroblewski P., 2010a, *ApJ*, 712, 964
- Güver T., Wroblewski P., Camarota L., Özel F., 2010b, *ApJ*, 719, 1807
- Haensel P., Potekhin A. Y., Yakovlev D. G., 2007, *Astrophysics and Space Science Library*, Vol. 326, *Neutron Stars 1: Equation of State and Structure*. Springer, New York
- Hasinger G., van der Klis M., 1989, *A&A*, 225, 79
- Hoffman J. A., Cominsky L., Lewin W. H. G., 1980, *ApJ*, 240, L27
- Inogamov N. A., Sunyaev R. A., 1999, *Astronomy Letters*, 25, 269
- Inogamov N. A., Sunyaev R. A., 2010, *Astronomy Letters*, 36, 848
- in’t Zand J. J. M., Jonker P. G., Markwardt C. B., 2007, *A&A*, 465, 953
- Jahoda K., Markwardt C. B., Radeva Y., Rots A. H., Stark M. J., Swank J. H., Strohmayer T. E., Zhang W., 2006, *ApJS*, 163, 401
- Ji L., Zhang S., Chen Y., Zhang S.-N., Torres D. F., Kretschmar P., Li J., 2014, *ApJ*, 782, 40
- Kuulkers E., den Hartog P. R., in’t Zand J. J. M., Verbunt F. W. M., Harris W. E., Cocchi M., 2003, *A&A*, 399, 663
- Kuulkers E., Homan J., van der Klis M., Lewin W. H. G., Méndez M., 2002, *A&A*, 382, 947
- Lapidus I. I., Sunyaev R. A., 1985, *MNRAS*, 217, 291
- Lattimer J. M., Prakash M., 2007, *Physics Reports*, 442, 109
- Lattimer J. M., Steiner A. W., 2014, *European Physical Journal A*, 50, 40

- Lewin W. H. G., van Paradijs J., Taam R. E., 1993, *Space Sci. Rev.*, 62, 223
- London R. A., Taam R. E., Howard W. M., 1986, *ApJ*, 306, 170
- Madej J., Joss P. C., Różańska A., 2004, *ApJ*, 602, 904
- Majczyna A., Madej J., Joss P. C., Różańska A., 2005, *A&A*, 430, 643
- Muno M. P., Galloway D. K., Chakrabarty D., 2004, *ApJ*, 608, 930
- Nakamura N., Dotani T., Inoue H., Mitsuda K., Tanaka Y., Matsuoka M., 1989, *PASJ*, 41, 617
- Özel F., Baym G., Güver T., 2010, *Physical Review D*, 82, 101301
- Özel F., Güver T., Psaltis D., 2009, *ApJ*, 693, 1775
- Patruno A., Watts A. L., 2012, arXiv:1206.2727
- Peille P., Olive J., Barret D., 2014, arXiv:1403.5471
- Piro A. L., Bildsten L., 2007, *ApJ*, 663, 1252
- Popham R., Sunyaev R., 2001, *ApJ*, 547, 355
- Poutanen J., Nättilä J., Kajava J. J. E., Latvala O.-M., Galloway D. K., Kuulkers E., Suleimanov V. F., 2014, arXiv:1405.2663
- Press W. H., Teukolsky S. A., Vetterling W. T., Flannery B. P., 2007, *Numerical recipes, The art of scientific computing*, Third edition. Cambridge University Press, Cambridge.
- Revnivtsev M. G., Suleimanov V. F., Poutanen J., 2013, *MNRAS*, 434, 2355
- Smale A. P., 1998, *ApJ*, 498, L141
- Steiner A. W., Lattimer J. M., Brown E. F., 2010, *ApJ*, 722, 33
- Stella L., Friedhorsky W., White N. E., 1987, *ApJ*, 312, L17
- Strohmayer T., Bildsten L., 2006, *New views of thermonuclear bursts*. pp 113–156
- Suleimanov V., Poutanen J., 2006, *MNRAS*, 369, 2036
- Suleimanov V., Poutanen J., Werner K., 2012, *A&A*, 545, A120
- Suleimanov V., Poutanen J., Revnivtsev M., Werner K., 2011a, *ApJ*, 742, 122
- Suleimanov V., Poutanen J., Werner K., 2011b, *A&A*, 527, A139
- Sztajno M., Fujimoto M. Y., van Paradijs J., Vacca W. D., Lewin W. H. G., Penninx W., Trumper J., 1987, *MNRAS*, 226, 39
- van Paradijs J., Dotani T., Tanaka Y., Tsuru T., 1990, *PASJ*, 42, 633
- van Paradijs J., Lewin W. H. G., 1987, *A&A*, 172, L20
- van Paradijs J., Penninx W., Lewin W. H. G., 1988, *MNRAS*, 233, 437
- van Straaten S., van der Klis M., Wijnands R., 2005, *ApJ*, 619, 455
- Watts A. L., 2012, *ARA&A*, 50, 609
- Weinberg N. N., Bildsten L., Schatz H., 2006, *ApJ*, 639, 1018
- Worpel H., Galloway D. K., Price D. J., 2013, *ApJ*, 772, 94
- Zhang G., Méndez M., Altamirano D., 2011, *MNRAS*, 413, 1913

APPENDIX A: A CATALOGUE OF PRE-BURSTS USED IN THIS STUDY

Table A1. A catalogue of PRE-bursts used in this study. The B# is the burst ID number used in this work and the bracketed (G8#) ID number used in Galloway et al. (2008) is also given for easier cross comparison. The touchdown fluxes F_{td} are in units of 10^{-7} erg cm $^{-2}$ s $^{-1}$, whereas the persistent flux is given in 10^{-9} erg cm $^{-2}$ s $^{-1}$ (1σ errors). HC and SC denote the hard- and the soft colours, respectively. The symbol a highlights the three differences with respect to the Galloway et al. (2008) catalogue: the burst #47 of 4U 1636–536 and the burst #42 of 4U 1728–34 were not classified as PRE bursts by Galloway et al. (2008) and the burst #34 of 4U 1728–34 was not in their catalogue at all.

B# (G8#)	OBSID	Date (MJD)	F_{td}	$K_{td/2}/K_{td}$	HC	SC	F_{per}
4U 1608–52							
1 (5)	30062-01-01-00	50899.587729	1.87 ± 0.02	1.08 ± 0.05	0.605 ± 0.008	1.45 ± 0.07	3.03 ± 0.07
2 (8)	30062-01-02-05	50914.275359	1.220 ± 0.015	3.2 ± 0.2	0.669 ± 0.014	1.54 ± 0.03	0.933 ± 0.010
3 (9)	50052-02-01-01	51612.031543	1.39 ± 0.03	1.7 ± 0.3	0.57 ± 0.05	1.4 ± 0.7	1.7 ± 0.5
4 (10)	50052-01-04-00	51614.071954	1.19 ± 0.02	3.8 ± 0.2	0.91 ± 0.02	1.66 ± 0.04	0.732 ± 0.010
5 (21)	70059-01-20-00	52524.102263	1.77 ± 0.03	1.06 ± 0.07	0.65 ± 0.03	1.3 ± 0.2	6.3 ± 0.7
6 (22)	70059-01-21-00	52526.160753	1.48 ± 0.02	1.01 ± 0.05	0.635 ± 0.008	1.55 ± 0.09	7.2 ± 0.2
7 (23)	70059-03-01-00	52529.180035	1.67 ± 0.06	1.04 ± 0.10	0.651 ± 0.008	1.54 ± 0.03	4.30 ± 0.04
8 (25)	70058-01-39-00	52536.318988	1.61 ± 0.02	1.58 ± 0.07	0.635 ± 0.014	1.48 ± 0.15	2.63 ± 0.13
9 (26)	70069-01-01-00	52542.501479	1.27 ± 0.02	3.8 ± 0.2	0.98 ± 0.02	1.38 ± 0.06	0.754 ± 0.012
10 (27)	70059-01-26-00	52546.900131	1.21 ± 0.03	3.3 ± 0.2	0.74 ± 0.02	1.60 ± 0.05	0.729 ± 0.011
11 (31)	90408-01-04-04	53104.408629	1.21 ± 0.05	3.4 ± 0.3	1.14 ± 0.02	1.56 ± 0.06	0.935 ± 0.011
12	93408-01-23-02	54434.974037	1.65 ± 0.04	1.34 ± 0.11	0.636 ± 0.012	1.57 ± 0.07	3.34 ± 0.08
13	93408-01-25-06	54452.116158	1.03 ± 0.03	3.9 ± 0.3	1.252 ± 0.015	1.69 ± 0.04	1.748 ± 0.013
14	93408-01-26-04	54461.031219	1.12 ± 0.02	4.9 ± 0.3	1.29 ± 0.04	1.8 ± 0.3	1.66 ± 0.08
15	93408-01-59-03	54692.075270	1.18 ± 0.03	3.9 ± 0.3	0.90 ± 0.02	1.28 ± 0.06	0.83 ± 0.02
16	95334-01-03-08	55270.220872	1.62 ± 0.04	1.32 ± 0.11	0.628 ± 0.014	1.4 ± 0.2	6.9 ± 0.4
17	96423-01-11-01	55725.155733	1.59 ± 0.03	0.94 ± 0.06	0.705 ± 0.010	1.55 ± 0.08	4.98 ± 0.12
18	96423-01-35-00	55890.371280	1.08 ± 0.02	4.2 ± 0.4	1.42 ± 0.04	1.86 ± 0.15	1.56 ± 0.03
4U 1636–536							
1 (1)	10088-01-07-02	50445.944732	0.714 ± 0.011	1.06 ± 0.07	0.708 ± 0.006	1.56 ± 0.06	4.42 ± 0.08
2 (3)	10088-01-08-01	50446.977634	0.604 ± 0.010	0.87 ± 0.06	0.703 ± 0.007	1.55 ± 0.06	4.07 ± 0.07
3 (4)	10088-01-08-03	50448.734636	0.681 ± 0.011	1.43 ± 0.10	0.726 ± 0.008	1.52 ± 0.06	4.41 ± 0.08
4 (6)	30053-02-02-02	51044.490033	0.750 ± 0.013	0.92 ± 0.07	0.725 ± 0.009	1.42 ± 0.08	4.02 ± 0.12
5 (7)	30053-02-01-02	51045.153577	0.77 ± 0.02	1.23 ± 0.09	0.728 ± 0.009	1.45 ± 0.08	4.03 ± 0.10
6 (9)	40028-01-02-00	51236.367009	0.707 ± 0.012	1.11 ± 0.08	0.702 ± 0.009	1.47 ± 0.06	3.81 ± 0.08
7 (10)	40028-01-04-00	51297.072674	0.689 ± 0.014	1.12 ± 0.09	0.674 ± 0.006	1.15 ± 0.06	5.6 ± 0.3
8 (12)	40028-01-06-00	51339.247576	0.683 ± 0.012	0.85 ± 0.06	0.717 ± 0.014	1.37 ± 0.13	3.4 ± 0.2
9 (13)	40028-01-08-00	51347.988936	0.563 ± 0.015	1.48 ± 0.14	0.718 ± 0.008	1.75 ± 0.09	5.04 ± 0.11
10 (14)	40030-03-04-00	51348.730536	0.675 ± 0.012	1.19 ± 0.08	0.707 ± 0.014	1.50 ± 0.14	3.7 ± 0.2
11 (15)	40031-01-01-06	51350.796442	0.654 ± 0.012	1.26 ± 0.08	0.720 ± 0.013	1.46 ± 0.12	3.69 ± 0.15
12 (16)	40028-01-10-00	51446.862370	0.409 ± 0.009	2.0 ± 0.2	0.771 ± 0.011	1.67 ± 0.12	7.8 ± 0.2
13 (20)	40028-01-15-00	51710.213022	0.79 ± 0.02	0.68 ± 0.05	0.729 ± 0.009	1.61 ± 0.08	4.05 ± 0.09
14 (21)	40028-01-18-00	51765.055325	0.637 ± 0.014	1.08 ± 0.09	0.738 ± 0.009	1.56 ± 0.08	3.84 ± 0.09
15 (22)	40028-01-18-00	51765.373534	0.75 ± 0.03	1.25 ± 0.15	0.727 ± 0.009	1.58 ± 0.07	3.63 ± 0.08
16 (23)	40028-01-19-00	51768.981502	0.765 ± 0.012	0.79 ± 0.05	0.731 ± 0.012	1.48 ± 0.12	3.59 ± 0.14
17 (24)	40028-01-20-00	51820.981815	0.723 ± 0.012	1.02 ± 0.07	0.723 ± 0.007	1.59 ± 0.04	3.37 ± 0.04
18 (25)	50030-02-01-00	51853.182628	0.579 ± 0.011	1.39 ± 0.10	0.698 ± 0.009	1.59 ± 0.10	4.59 ± 0.13
19 (26)	50030-02-02-00	51860.752408	0.609 ± 0.011	1.09 ± 0.08	0.705 ± 0.007	1.76 ± 0.06	4.89 ± 0.07
20 (27)	50030-02-04-00	51937.116815	0.63 ± 0.02	1.16 ± 0.10	0.723 ± 0.010	1.52 ± 0.09	3.79 ± 0.11
21 (28)	50030-02-05-01	51941.876280	0.637 ± 0.011	1.08 ± 0.08	0.69 ± 0.02	1.5 ± 0.2	4.3 ± 0.2
22 (29)	50030-02-05-00	51942.100935	0.68 ± 0.02	1.32 ± 0.11	0.720 ± 0.012	1.45 ± 0.12	4.1 ± 0.2
23 (30)	50030-02-09-00	52004.713947	1.06 ± 0.02	1.18 ± 0.09	0.752 ± 0.013	1.54 ± 0.08	3.68 ± 0.09
24 (31)	50030-02-10-00	52029.228869	0.76 ± 0.03	0.99 ± 0.10	0.712 ± 0.015	1.46 ± 0.14	2.76 ± 0.13
25 (34)	60032-01-02-00	52075.135469	0.76 ± 0.02	1.35 ± 0.12	0.758 ± 0.012	1.60 ± 0.05	2.07 ± 0.03
26 (38)	60032-01-06-01	52149.279399	0.647 ± 0.011	1.13 ± 0.08	0.724 ± 0.010	1.60 ± 0.08	3.13 ± 0.07
27 (45)	60032-01-12-00	52182.616870	0.781 ± 0.015	1.15 ± 0.08	0.71 ± 0.02	1.52 ± 0.14	2.60 ± 0.11
28 (49)	60032-01-14-01	52214.318968	0.701 ± 0.014	1.12 ± 0.09	0.73 ± 0.02	1.5 ± 0.2	3.2 ± 0.2
29 (50)	60032-01-18-00	52273.691505	0.541 ± 0.011	2.07 ± 0.14	0.82 ± 0.02	1.60 ± 0.11	1.79 ± 0.06
30 (61)	60032-01-20-00	52283.019196	0.84 ± 0.02	1.13 ± 0.08	0.778 ± 0.010	1.60 ± 0.02	2.08 ± 0.02
31 (62)	60032-01-20-01	52283.534309	0.736 ± 0.014	0.98 ± 0.07	0.731 ± 0.015	1.60 ± 0.10	2.15 ± 0.06
32 (68)	60032-05-01-00	52286.054732	0.599 ± 0.010	1.68 ± 0.11	0.937 ± 0.012	1.67 ± 0.03	1.52 ± 0.02
33 (72)	60032-05-02-00	52286.555354	0.686 ± 0.014	1.28 ± 0.10	0.936 ± 0.014	1.63 ± 0.03	1.65 ± 0.02
34 (79)	60032-05-04-00	52287.522590	0.541 ± 0.009	1.72 ± 0.12	0.939 ± 0.013	1.65 ± 0.02	1.611 ± 0.015

Table A1 – continued

B# (G8#)	OBSID	Date (MJD)	F_{td}	$K_{td/2}/K_{td}$	HC	SC	F_{per}
35 (86)	60032-05-06-00	52288.515004	0.80 ± 0.02	1.23 ± 0.11	0.804 ± 0.011	1.61 ± 0.02	1.896 ± 0.015
36 (87)	60032-05-07-00	52288.975073	0.632 ± 0.008	1.84 ± 0.10	0.873 ± 0.011	1.57 ± 0.04	1.69 ± 0.02
37 (88)	60032-05-07-01	52289.293513	0.568 ± 0.011	1.94 ± 0.14	0.896 ± 0.013	1.61 ± 0.04	1.60 ± 0.02
38 (94)	60032-05-09-00	52289.977634	0.663 ± 0.015	1.53 ± 0.11	0.841 ± 0.010	1.56 ± 0.04	1.75 ± 0.02
39 (109)	60032-05-12-00	52304.963829	0.629 ± 0.011	1.02 ± 0.07	0.669 ± 0.014	1.14 ± 0.14	5.3 ± 0.4
40 (110)	60032-05-13-00	52310.932538	0.72 ± 0.03	0.88 ± 0.10	0.719 ± 0.010	1.67 ± 0.10	4.86 ± 0.12
41 (111)	60032-05-14-00	52316.733415	0.71 ± 0.02	1.39 ± 0.14	0.705 ± 0.007	1.68 ± 0.05	4.45 ± 0.06
42 (115)	60032-05-18-00	52390.214092	0.561 ± 0.012	1.39 ± 0.13	0.75 ± 0.02	1.7 ± 0.2	3.0 ± 0.2
43 (122)	60032-05-22-00	52551.251902	0.629 ± 0.013	1.53 ± 0.12	0.811 ± 0.012	1.59 ± 0.08	3.08 ± 0.08
44 (125)	80425-01-01-00	52899.945004	0.665 ± 0.014	1.82 ± 0.13	0.96 ± 0.02	1.60 ± 0.05	1.48 ± 0.02
45 (136)	91024-01-42-00	53516.313817	0.75 ± 0.02	1.14 ± 0.10	0.732 ± 0.012	1.59 ± 0.06	2.23 ± 0.04
46 (137)	91024-01-46-00	53524.389520	0.694 ± 0.011	1.22 ± 0.08	0.742 ± 0.009	1.62 ± 0.05	2.51 ± 0.04
47 (148) ^a	91024-01-80-00	53592.234454	0.726 ± 0.012	1.18 ± 0.08	0.725 ± 0.006	1.58 ± 0.02	3.67 ± 0.03
48 (149)	91024-01-82-00	53596.088511	0.65 ± 0.02	1.28 ± 0.13	0.693 ± 0.012	1.58 ± 0.13	4.9 ± 0.2
49 (150)	91024-01-83-00	53598.074040	0.71 ± 0.02	0.77 ± 0.07	0.710 ± 0.010	1.68 ± 0.11	4.83 ± 0.13
50 (168)	91024-01-30-10	53688.952608	0.79 ± 0.02	1.08 ± 0.10	0.711 ± 0.011	1.50 ± 0.10	4.08 ± 0.13
51	91152-05-02-00	53919.074680	0.71 ± 0.02	1.21 ± 0.11	0.759 ± 0.011	1.47 ± 0.11	4.15 ± 0.14
52	92023-01-72-00	53940.493218	0.694 ± 0.014	0.90 ± 0.06	0.718 ± 0.012	1.50 ± 0.12	3.26 ± 0.12
53	92023-01-10-10	54012.556123	0.63 ± 0.02	1.48 ± 0.14	0.697 ± 0.008	1.71 ± 0.03	3.70 ± 0.04
54	92023-01-29-10	54050.902738	0.72 ± 0.02	1.07 ± 0.10	0.72 ± 0.02	1.47 ± 0.14	2.37 ± 0.11
55	92023-01-31-10	54054.249711	0.672 ± 0.013	1.12 ± 0.09	0.72 ± 0.02	1.5 ± 0.2	2.8 ± 0.2
56	92023-01-60-10	54112.003181	0.76 ± 0.02	1.15 ± 0.10	0.73 ± 0.02	1.5 ± 0.2	2.56 ± 0.13
57	92023-01-23-20	54222.420545	0.712 ± 0.014	1.18 ± 0.09	0.719 ± 0.008	1.56 ± 0.06	4.31 ± 0.08
58	70036-01-02-01	54271.044500	0.786 ± 0.015	0.91 ± 0.07	0.719 ± 0.014	1.59 ± 0.11	2.77 ± 0.09
59	70036-01-02-00	54272.092498	0.77 ± 0.02	0.96 ± 0.08	0.715 ± 0.010	1.57 ± 0.05	2.90 ± 0.05
60	93091-01-01-00	54371.719668	0.711 ± 0.014	1.17 ± 0.09	0.777 ± 0.013	1.55 ± 0.02	1.81 ± 0.02
61	93087-01-69-00	54416.318415	0.73 ± 0.02	1.30 ± 0.12	0.72 ± 0.02	1.5 ± 0.2	2.2 ± 0.2
62	93087-01-24-10	54522.687075	0.78 ± 0.03	1.5 ± 0.2	0.79 ± 0.03	1.3 ± 0.3	2.3 ± 0.2
63	93091-01-02-00	54523.579098	0.70 ± 0.02	1.4 ± 0.2	0.722 ± 0.015	1.63 ± 0.08	2.70 ± 0.06
64	93087-01-28-10	54530.797894	0.65 ± 0.02	1.18 ± 0.12	0.731 ± 0.014	1.57 ± 0.10	2.49 ± 0.08
65	93087-01-57-10	54588.165192	0.792 ± 0.015	0.96 ± 0.07	0.814 ± 0.011	1.53 ± 0.02	2.44 ± 0.02
66	93087-01-70-10	54614.815982	0.68 ± 0.02	0.98 ± 0.10	0.71 ± 0.02	1.4 ± 0.3	3.1 ± 0.3
67	93087-01-91-10	54656.604263	0.74 ± 0.02	1.02 ± 0.10	0.72 ± 0.02	1.6 ± 0.3	2.5 ± 0.2
68	93087-01-04-20	54678.268528	0.76 ± 0.02	1.07 ± 0.10	0.770 ± 0.014	1.60 ± 0.09	2.32 ± 0.06
69	94310-01-01-00	54904.833592	0.710 ± 0.014	1.16 ± 0.09	0.744 ± 0.009	1.59 ± 0.03	2.30 ± 0.02
70	94310-01-03-00	55079.220357	0.67 ± 0.02	1.01 ± 0.10	0.72 ± 0.02	1.59 ± 0.12	2.16 ± 0.08
71	94087-01-45-10	55110.235681	0.72 ± 0.02	1.2 ± 0.2	0.71 ± 0.02	1.66 ± 0.11	2.70 ± 0.09
72	94087-01-73-10	55166.027634	0.598 ± 0.015	1.9 ± 0.2	0.702 ± 0.014	1.51 ± 0.13	3.73 ± 0.15
73	94087-01-74-10	55168.322805	0.72 ± 0.02	0.94 ± 0.09	0.713 ± 0.013	1.61 ± 0.12	4.22 ± 0.14
74	95087-01-39-00	55274.497261	0.64 ± 0.02	2.2 ± 0.2	0.790 ± 0.015	1.58 ± 0.04	1.59 ± 0.02
75	95087-01-42-00	55280.541745	0.526 ± 0.014	1.4 ± 0.2	0.71 ± 0.03	1.6 ± 0.3	2.6 ± 0.2
76	93082-06-06-00	55356.990762	0.70 ± 0.02	1.44 ± 0.15	0.71 ± 0.02	1.7 ± 0.2	5.0 ± 0.2
77	95087-01-89-00	55374.685875	0.76 ± 0.02	2.0 ± 0.2	0.74 ± 0.02	1.5 ± 0.2	1.83 ± 0.15
78	95087-01-01-10	55394.904737	0.65 ± 0.02	3.0 ± 0.3	0.80 ± 0.02	1.53 ± 0.13	1.51 ± 0.06
79	95087-01-22-10	55436.152747	0.61 ± 0.02	1.39 ± 0.15	0.709 ± 0.012	1.71 ± 0.10	3.65 ± 0.10
80	96087-01-46-00	55652.641696	0.74 ± 0.03	1.07 ± 0.14	0.711 ± 0.015	1.60 ± 0.07	2.76 ± 0.06
81	96087-01-50-10	55857.000487	0.77 ± 0.02	1.18 ± 0.10	0.81 ± 0.02	1.57 ± 0.13	2.78 ± 0.10
4U 1702–429							
1 (11)	50025-01-01-00	51781.333039	0.813 ± 0.015	2.15 ± 0.13	1.003 ± 0.012	1.99 ± 0.05	1.37 ± 0.02
2 (19)	80033-01-01-08	52957.629763	0.89 ± 0.02	2.4 ± 0.2	1.148 ± 0.014	1.57 ± 0.04	1.749 ± 0.015
3 (43)	80033-01-19-04	53211.964665	0.80 ± 0.02	2.2 ± 0.2	1.01 ± 0.03	1.8 ± 0.2	1.52 ± 0.05
4 (44)	80033-01-20-02	53212.794286	0.86 ± 0.02	2.21 ± 0.15	1.05 ± 0.02	1.97 ± 0.09	1.38 ± 0.02
5 (45)	80033-01-21-00	53311.806086	0.76 ± 0.02	2.3 ± 0.2	0.92 ± 0.04	1.50 ± 0.13	1.38 ± 0.04
4U 1705–44							
1 (1)	20074-02-01-00	50495.947813	0.397 ± 0.008	1.17 ± 0.09	0.654 ± 0.013	1.7 ± 0.2	2.50 ± 0.11
2 (5)	20073-04-01-03	50542.503568	0.401 ± 0.008	1.25 ± 0.09	0.670 ± 0.008	1.72 ± 0.07	2.58 ± 0.04
3 (21)	40034-01-05-00	51333.396013	0.430 ± 0.010	1.04 ± 0.10	0.637 ± 0.008	1.86 ± 0.06	2.54 ± 0.03
4	93060-01-25-10	54764.450160	0.363 ± 0.012	1.6 ± 0.2	0.66 ± 0.02	1.7 ± 0.2	2.70 ± 0.14
5	93060-01-28-10	54776.944564	0.369 ± 0.012	1.8 ± 0.2	0.76 ± 0.02	1.8 ± 0.2	1.30 ± 0.05

Table A1 – continued

B# (G8#)	OBSID	Date (MJD)	F_{td}	$K_{td/2}/K_{td}$	HC	SC	F_{per}
4U 1724–307							
1 (1)	10090-01-01-02	50395.292725	0.624 ± 0.011	2.66 ± 0.15	1.200 ± 0.013	1.63 ± 0.03	1.408 ± 0.009
2 (2)	80138-06-06-00	53058.402090	0.429 ± 0.010	1.06 ± 0.10	0.74 ± 0.02	1.9 ± 0.2	2.21 ± 0.11
3 (3)	90058-06-02-00	53147.218979	0.603 ± 0.012	1.69 ± 0.12	0.83 ± 0.02	1.8 ± 0.2	1.36 ± 0.05
4	93044-06-04-00	54526.679905	0.65 ± 0.02	2.3 ± 0.2	1.22 ± 0.02	1.66 ± 0.06	1.511 ± 0.015
4U 1728–34							
1 (8)	10073-01-04-00	50131.895744	0.90 ± 0.02	1.36 ± 0.10	1.005 ± 0.011	1.88 ± 0.08	3.57 ± 0.05
2 (9)	10073-01-06-00	50135.965429	1.06 ± 0.02	2.13 ± 0.14	1.107 ± 0.009	2.03 ± 0.03	2.77 ± 0.02
3 (10)	10073-01-07-00	50137.241242	1.03 ± 0.03	2.1 ± 0.2	1.131 ± 0.010	2.05 ± 0.04	2.65 ± 0.02
4 (21)	20083-01-04-01	50718.472324	0.91 ± 0.02	1.23 ± 0.08	0.933 ± 0.012	1.96 ± 0.10	3.12 ± 0.05
5 (22)	20083-01-04-01	50718.663265	0.810 ± 0.013	1.13 ± 0.06	0.890 ± 0.007	1.99 ± 0.04	3.24 ± 0.02
6 (27)	30042-03-01-00	51086.423580	1.01 ± 0.02	1.34 ± 0.15	1.208 ± 0.008	2.09 ± 0.03	4.93 ± 0.03
7 (28)	30042-03-03-01	51110.106607	0.96 ± 0.02	1.5 ± 0.2	1.216 ± 0.008	2.03 ± 0.04	4.44 ± 0.03
8 (29)	30042-03-06-00	51118.158997	1.04 ± 0.02	1.4 ± 0.2	1.232 ± 0.015	2.4 ± 0.2	4.49 ± 0.09
9 (30)	30042-03-06-00	51118.291829	0.98 ± 0.02	1.6 ± 0.2	1.232 ± 0.009	2.01 ± 0.04	4.85 ± 0.04
10 (31)	30042-03-07-01	51119.947246	0.99 ± 0.02	1.7 ± 0.2	1.218 ± 0.010	1.99 ± 0.05	4.77 ± 0.04
11 (32)	30042-03-07-00	51120.085727	1.00 ± 0.02	1.4 ± 0.2	1.19 ± 0.02	2.06 ± 0.14	4.88 ± 0.08
12 (33)	30042-03-10-00	51127.815762	0.94 ± 0.02	1.7 ± 0.2	1.183 ± 0.008	2.06 ± 0.03	4.98 ± 0.03
13 (34)	30042-03-11-00	51128.026800	0.98 ± 0.02	1.6 ± 0.2	1.173 ± 0.007	2.07 ± 0.03	4.90 ± 0.03
14 (35)	30042-03-12-00	51128.681711	0.95 ± 0.02	1.19 ± 0.13	1.158 ± 0.008	2.09 ± 0.03	4.89 ± 0.03
15 (36)	30042-03-12-00	51128.814665	0.95 ± 0.02	1.33 ± 0.15	1.149 ± 0.008	2.10 ± 0.03	4.85 ± 0.03
16 (37)	30042-03-13-00	51129.014549	0.94 ± 0.02	1.35 ± 0.15	1.11 ± 0.04	1.8 ± 0.3	5.3 ± 0.3
17 (38)	30042-03-14-00	51133.424633	0.92 ± 0.02	0.78 ± 0.09	0.974 ± 0.007	2.06 ± 0.04	5.01 ± 0.03
18 (39)	30042-03-15-00	51133.673684	0.88 ± 0.02	1.16 ± 0.15	0.995 ± 0.006	2.09 ± 0.03	4.81 ± 0.03
19 (41)	30042-03-17-00	51134.573024	0.96 ± 0.02	1.13 ± 0.13	1.113 ± 0.007	2.10 ± 0.03	4.26 ± 0.03
20 (43)	30042-03-20-00	51196.991395	1.06 ± 0.02	1.9 ± 0.2	1.216 ± 0.009	2.00 ± 0.04	3.69 ± 0.03
21 (44)	40033-06-01-00	51198.144072	1.09 ± 0.03	1.68 ± 0.11	1.200 ± 0.012	1.99 ± 0.08	3.95 ± 0.03
22 (45)	40033-06-02-00	51200.267845	0.96 ± 0.02	1.39 ± 0.08	1.171 ± 0.008	2.05 ± 0.04	4.21 ± 0.03
23 (46)	40033-06-02-01	51201.993076	0.89 ± 0.02	1.59 ± 0.12	1.122 ± 0.008	2.08 ± 0.04	4.32 ± 0.03
24 (47)	40033-06-02-02	51202.358973	0.86 ± 0.02	1.89 ± 0.12	1.126 ± 0.008	2.12 ± 0.03	4.29 ± 0.03
25 (48)	40033-06-02-03	51204.001838	0.89 ± 0.02	1.20 ± 0.08	1.043 ± 0.007	2.09 ± 0.04	4.43 ± 0.03
26 (49)	40033-06-02-03	51204.130600	0.87 ± 0.02	1.14 ± 0.09	1.038 ± 0.007	2.10 ± 0.04	4.45 ± 0.03
27 (51)	40033-06-02-05	51206.141372	0.880 ± 0.014	1.21 ± 0.07	1.051 ± 0.010	2.08 ± 0.07	4.13 ± 0.03
28 (52)	40033-06-03-01	51208.985938	1.02 ± 0.02	1.44 ± 0.10	1.053 ± 0.008	2.10 ± 0.04	3.76 ± 0.03
29 (53)	40033-06-03-02	51209.918759	0.80 ± 0.02	1.34 ± 0.09	0.935 ± 0.013	1.89 ± 0.12	4.14 ± 0.09
30 (54)	40033-06-03-02	51210.083146	0.81 ± 0.02	1.08 ± 0.08	0.948 ± 0.006	2.06 ± 0.03	4.06 ± 0.02
31 (55)	40033-06-03-05	51213.939185	0.864 ± 0.013	0.98 ± 0.05	0.929 ± 0.014	1.92 ± 0.13	3.76 ± 0.08
32 (56)	40027-06-01-00	51236.792781	0.93 ± 0.02	1.81 ± 0.10	1.091 ± 0.009	2.06 ± 0.04	2.67 ± 0.02
33 (57)	40027-06-01-02	51237.203189	0.87 ± 0.02	1.39 ± 0.08	1.086 ± 0.009	2.04 ± 0.04	2.69 ± 0.02
34 (...)	40027-06-01-06	51238.566977	0.92 ± 0.02	1.70 ± 0.10	1.094 ± 0.011	2.02 ± 0.04	2.75 ± 0.02
35 (58)	40027-06-01-03	51238.792243	0.99 ± 0.02	1.83 ± 0.12	1.125 ± 0.011	2.02 ± 0.06	2.75 ± 0.02
36 (59)	40027-06-01-08	51240.047298	0.919 ± 0.015	1.65 ± 0.08	1.100 ± 0.009	2.07 ± 0.04	2.89 ± 0.02
37 (62)	40027-08-01-01	51359.827252	0.93 ± 0.02	1.46 ± 0.09	1.087 ± 0.012	2.05 ± 0.06	2.89 ± 0.03
38 (63)	40027-08-03-00	51369.422561	1.07 ± 0.02	1.62 ± 0.12	1.156 ± 0.012	1.94 ± 0.08	2.99 ± 0.04
39 (69)	40019-03-01-00	51443.014309	0.83 ± 0.02	1.17 ± 0.08	0.957 ± 0.010	2.08 ± 0.05	3.14 ± 0.03
40 (76)	50029-23-02-01	51657.203959	0.93 ± 0.02	2.02 ± 0.13	1.107 ± 0.009	2.00 ± 0.04	2.54 ± 0.02
41 (77)	50029-23-02-02	51657.679170	1.04 ± 0.02	1.58 ± 0.10	1.094 ± 0.010	2.04 ± 0.05	2.56 ± 0.02
42 (78) ^a	50023-01-21-00	51691.713212	1.00 ± 0.03	1.85 ± 0.13	1.179 ± 0.015	1.61 ± 0.05	3.61 ± 0.04
43 (79)	50023-01-22-00	51695.340412	1.05 ± 0.02	1.98 ± 0.13	1.136 ± 0.012	2.00 ± 0.06	3.02 ± 0.03
44 (80)	50023-01-23-00	51697.479960	1.01 ± 0.02	2.10 ± 0.14	1.11 ± 0.02	2.02 ± 0.12	3.15 ± 0.04
45 (82)	50030-03-02-00	51942.946777	0.94 ± 0.02	1.49 ± 0.11	0.880 ± 0.010	2.04 ± 0.06	1.85 ± 0.02
46 (83)	50030-03-03-02	51949.126690	1.09 ± 0.03	2.3 ± 0.2	1.19 ± 0.02	1.87 ± 0.08	1.80 ± 0.03
47 (85)	50030-03-04-00	52007.613823	0.82 ± 0.04	1.06 ± 0.13	1.010 ± 0.008	2.10 ± 0.04	3.85 ± 0.03
48 (86)	50030-03-04-02	52008.087790	0.842 ± 0.015	1.08 ± 0.06	0.906 ± 0.007	2.04 ± 0.04	4.33 ± 0.03
49 (87)	50030-03-05-03	52024.438632	1.10 ± 0.03	2.22 ± 0.15	1.18 ± 0.02	1.97 ± 0.08	3.11 ± 0.04
50 (88)	50030-03-05-02	52024.696132	1.05 ± 0.02	2.8 ± 0.2	1.20 ± 0.02	1.92 ± 0.08	2.98 ± 0.05
51 (89)	60029-02-01-00	52056.408693	1.07 ± 0.03	1.82 ± 0.15	0.959 ± 0.008	2.03 ± 0.04	4.42 ± 0.04
52 (91)	50030-03-06-00	52112.254234	1.06 ± 0.02	2.05 ± 0.12	1.036 ± 0.012	1.97 ± 0.05	1.83 ± 0.02

Table A1 – continued

B# (G8#)	OBSID	Date (MJD)	F_{td}	$K_{td/2}/K_{td}$	HC	SC	F_{per}
53 (92)	50030-03-06-02	52112.585290	1.05 ± 0.05	1.9 ± 0.2	1.085 ± 0.013	1.96 ± 0.06	1.76 ± 0.02
54 (97)	70028-01-01-07	52336.211931	0.82 ± 0.02	1.24 ± 0.08	1.04 ± 0.010	2.07 ± 0.05	3.25 ± 0.03
55 (100)	70028-01-01-02	52337.098108	0.85 ± 0.02	1.39 ± 0.11	1.02 ± 0.02	2.02 ± 0.08	3.22 ± 0.05
56 (101)	70028-01-01-00	52337.946352	0.90 ± 0.03	1.52 ± 0.13	1.027 ± 0.014	2.06 ± 0.10	3.08 ± 0.04
57 (102)	70028-01-01-00	52338.091517	0.84 ± 0.02	1.19 ± 0.09	1.02 ± 0.03	1.8 ± 0.3	3.18 ± 0.15
58 (104)	70028-01-01-12	52338.416621	0.88 ± 0.02	1.60 ± 0.11	1.097 ± 0.014	2.04 ± 0.09	2.94 ± 0.03
59	92023-03-03-00	53802.039063	0.90 ± 0.03	1.52 ± 0.13	1.108 ± 0.012	2.01 ± 0.07	3.43 ± 0.03
60	92023-03-35-00	53866.028019	0.99 ± 0.02	1.86 ± 0.12	1.107 ± 0.012	2.00 ± 0.05	3.51 ± 0.03
61	92023-03-02-10	53996.503670	0.95 ± 0.02	1.9 ± 0.2	1.17 ± 0.03	1.9 ± 0.3	3.9 ± 0.2
62	92023-03-06-10	54004.550617	0.86 ± 0.02	1.10 ± 0.10	1.046 ± 0.009	2.10 ± 0.05	5.99 ± 0.05
63	92023-03-16-10	54024.205142	0.83 ± 0.02	0.82 ± 0.07	0.957 ± 0.015	1.95 ± 0.12	3.49 ± 0.07
64	92023-03-20-10	54032.060987	0.88 ± 0.02	0.86 ± 0.05	0.870 ± 0.012	1.96 ± 0.11	4.54 ± 0.08
65	92023-03-27-10	54046.469298	0.77 ± 0.02	1.28 ± 0.10	0.961 ± 0.011	1.98 ± 0.09	5.93 ± 0.07
66	92023-03-31-10	54054.205976	0.93 ± 0.03	1.51 ± 0.12	1.137 ± 0.011	2.02 ± 0.06	3.71 ± 0.04
67	92023-03-34-10	54120.259567	1.04 ± 0.07	2.0 ± 0.3	1.131 ± 0.011	1.97 ± 0.05	2.51 ± 0.02
68	92023-03-44-10	54140.744318	0.90 ± 0.02	1.50 ± 0.10	1.121 ± 0.011	2.03 ± 0.05	3.91 ± 0.04
69	92023-03-44-00	54166.219564	0.98 ± 0.03	2.1 ± 0.2	1.147 ± 0.014	2.01 ± 0.06	3.59 ± 0.04
70	92023-03-70-00	54226.783693	0.93 ± 0.02	2.24 ± 0.15	1.159 ± 0.011	2.05 ± 0.06	3.70 ± 0.04
71	92023-03-71-00	54228.071109	0.90 ± 0.02	1.69 ± 0.14	1.097 ± 0.012	2.06 ± 0.05	4.31 ± 0.04
72	92023-03-73-00	54230.488444	0.94 ± 0.02	1.55 ± 0.12	1.124 ± 0.012	2.04 ± 0.06	4.57 ± 0.05
73	92023-03-66-10	54234.897703	0.90 ± 0.03	1.9 ± 0.2	1.15 ± 0.03	2.0 ± 0.2	5.05 ± 0.11
74	92023-03-83-10	54268.409381	1.00 ± 0.03	1.9 ± 0.2	1.009 ± 0.010	2.05 ± 0.06	4.14 ± 0.04
75	95337-01-02-00	55473.926815	0.96 ± 0.02	1.15 ± 0.07	0.785 ± 0.011	2.03 ± 0.07	2.38 ± 0.04
76	96322-01-05-02	55840.957370	1.01 ± 0.04	1.6 ± 0.2	1.19 ± 0.02	2.00 ± 0.08	3.60 ± 0.05
77	96322-01-05-00	55841.140924	0.99 ± 0.02	1.91 ± 0.14	1.20 ± 0.02	2.00 ± 0.10	3.62 ± 0.05
78	96322-01-05-00	55841.301314	1.03 ± 0.03	2.2 ± 0.2	1.18 ± 0.06	1.7 ± 0.4	4.0 ± 0.3
79	96322-01-05-00	55841.477828	1.04 ± 0.03	1.72 ± 0.13	1.20 ± 0.03	1.8 ± 0.2	3.73 ± 0.12
4U 1735–44							
1 (3)	20084-01-02-04	50693.542191	0.390 ± 0.008	0.90 ± 0.07	0.84 ± 0.02	1.7 ± 0.2	5.2 ± 0.2
2 (6)	30056-02-01-00	50963.430507	0.354 ± 0.009	1.02 ± 0.10	0.949 ± 0.010	1.88 ± 0.05	3.19 ± 0.03
3 (7)	30056-02-01-00	50963.490137	0.334 ± 0.007	0.99 ± 0.08	0.938 ± 0.009	1.84 ± 0.06	3.24 ± 0.04
4 (8)	30056-02-01-00	50963.547509	0.283 ± 0.006	0.92 ± 0.08	0.933 ± 0.007	1.86 ± 0.03	3.20 ± 0.02
5 (10)	40030-02-01-00	51347.126951	0.340 ± 0.010	1.38 ± 0.12	0.94 ± 0.04	1.9 ± 0.5	3.6 ± 0.4
6 (11)	40031-02-01-04	51348.108487	0.368 ± 0.009	0.88 ± 0.08	0.87 ± 0.03	1.5 ± 0.3	4.4 ± 0.4
7	91025-01-10-01	54727.956277	0.360 ± 0.012	0.95 ± 0.12	0.926 ± 0.013	1.85 ± 0.08	3.44 ± 0.06
8	91025-01-11-00	54728.905009	0.393 ± 0.012	0.85 ± 0.12	0.901 ± 0.010	1.93 ± 0.06	4.30 ± 0.05
9	93200-01-01-03	54879.335374	0.438 ± 0.014	1.00 ± 0.12	1.06 ± 0.03	2.04 ± 0.14	2.10 ± 0.04
10	93200-01-01-02	54879.855383	0.339 ± 0.013	1.8 ± 0.2	1.068 ± 0.012	1.93 ± 0.03	2.37 ± 0.02
11	93200-01-02-00	54974.580901	0.407 ± 0.013	1.16 ± 0.14	0.894 ± 0.014	1.94 ± 0.11	3.59 ± 0.07
12	93200-01-02-00	54974.783684	0.377 ± 0.012	0.83 ± 0.11	0.87 ± 0.02	2.0 ± 0.2	3.8 ± 0.2
13	93200-01-03-01	55123.323892	0.446 ± 0.013	0.75 ± 0.10	0.95 ± 0.02	1.86 ± 0.11	3.08 ± 0.07
4U 1820–30							
1 (1)	20075-01-05-00	50570.731795	0.59 ± 0.02	1.55 ± 0.14	1.033 ± 0.007	1.79 ± 0.02	3.683 ± 0.015
2 (2)	40017-01-24-00	52794.738826	0.621 ± 0.015	1.53 ± 0.12	1.161 ± 0.009	1.97 ± 0.03	2.93 ± 0.02
3 (3)	70030-03-04-01	52802.076265	0.59 ± 0.02	1.38 ± 0.12	1.145 ± 0.009	1.97 ± 0.03	2.92 ± 0.02
4 (4)	70030-03-05-01	52805.896358	0.609 ± 0.014	1.45 ± 0.13	1.145 ± 0.010	1.95 ± 0.02	3.81 ± 0.02
5 (5)	90027-01-03-05	53277.439257	0.628 ± 0.013	1.46 ± 0.11	1.015 ± 0.008	1.81 ± 0.04	3.83 ± 0.04
6	94090-01-01-02	54948.821939	0.60 ± 0.02	1.6 ± 0.2	1.111 ± 0.015	1.97 ± 0.04	3.58 ± 0.04
7	94090-01-01-05	54950.703513	0.58 ± 0.02	1.36 ± 0.13	1.18 ± 0.02	1.96 ± 0.11	3.44 ± 0.05
8	94090-01-02-03	54956.775426	0.59 ± 0.02	1.43 ± 0.15	1.24 ± 0.02	2.01 ± 0.11	3.28 ± 0.05
9	94090-01-02-02	54958.740672	0.61 ± 0.02	1.50 ± 0.15	1.25 ± 0.03	2.1 ± 0.2	3.09 ± 0.09
10	94090-01-04-00	54978.322182	0.63 ± 0.02	1.8 ± 0.2	1.27 ± 0.03	1.9 ± 0.2	3.75 ± 0.10
11	94090-01-04-01	54978.495588	0.61 ± 0.02	1.28 ± 0.14	1.33 ± 0.02	2.03 ± 0.06	3.52 ± 0.03
12	94090-01-05-00	54981.187938	0.614 ± 0.015	1.57 ± 0.12	1.28 ± 0.02	2.00 ± 0.12	4.05 ± 0.06
13	94090-02-01-00	54994.534879	0.58 ± 0.02	1.15 ± 0.13	1.185 ± 0.012	1.99 ± 0.03	5.84 ± 0.06
14	94090-02-01-00	54994.613713	0.53 ± 0.02	1.03 ± 0.11	1.130 ± 0.015	1.91 ± 0.09	6.10 ± 0.12
15	96090-01-01-00	55624.881378	0.58 ± 0.02	1.41 ± 0.14	1.15 ± 0.02	2.01 ± 0.11	2.95 ± 0.05
16	96090-01-01-02	55626.774306	0.55 ± 0.02	1.28 ± 0.14	0.912 ± 0.009	1.78 ± 0.07	4.67 ± 0.08

Table A1 – *continued*

B# (G8#)	OBSID	Date (MJD)	F_{td}	$K_{td/2}/K_{td}$	HC	SC	F_{per}
Aql X-1							
1 (4)	20098-03-08-00	50508.977504	1.22 ± 0.02	1.32 ± 0.07	0.505 ± 0.008	1.44 ± 0.02	1.37 ± 0.02
2 (5)	20092-01-05-00	50696.524280	1.21 ± 0.02	0.95 ± 0.05	0.521 ± 0.007	1.43 ± 0.06	3.56 ± 0.07
3 (6)	20092-01-05-03	50699.400018	0.650 ± 0.009	1.17 ± 0.07	0.503 ± 0.005	1.53 ± 0.02	3.31 ± 0.02
4 (10)	40047-03-02-00	51332.780597	1.31 ± 0.02	1.12 ± 0.06	0.562 ± 0.012	1.44 ± 0.08	2.60 ± 0.08
5 (11)	40047-03-06-00	51336.591439	1.20 ± 0.04	1.9 ± 0.2	0.467 ± 0.012	1.54 ± 0.07	1.05 ± 0.03
6 (19)	50049-02-13-01	51856.157590	0.75 ± 0.02	1.63 ± 0.13	0.526 ± 0.006	1.59 ± 0.06	7.77 ± 0.15
7 (28)	60429-01-06-00	52324.991248	1.22 ± 0.02	0.93 ± 0.05	0.553 ± 0.006	1.52 ± 0.03	2.53 ± 0.03
8 (29)	70069-03-02-03	52347.182990	0.668 ± 0.013	1.9 ± 0.2	0.514 ± 0.006	1.55 ± 0.05	3.71 ± 0.06
9	92438-01-02-01	54259.248574	1.18 ± 0.03	3.7 ± 0.3	1.23 ± 0.04	1.67 ± 0.05	0.355 ± 0.006
10	93405-01-03-07	54365.807784	0.85 ± 0.03	0.77 ± 0.09	0.583 ± 0.009	1.42 ± 0.11	6.7 ± 0.3
11	94076-01-05-02	55157.140116	1.11 ± 0.02	1.12 ± 0.07	0.538 ± 0.006	1.53 ± 0.05	5.53 ± 0.13
12	96440-01-09-07	55904.228389	1.13 ± 0.03	2.0 ± 0.2	0.56 ± 0.02	1.44 ± 0.08	1.26 ± 0.04
HETE J1900.1–2455							
1 (1)	91059-03-01-04	53572.959405	1.234 ± 0.014	4.5 ± 0.2	1.6 ± 0.2	1.59 ± 0.08	0.723 ± 0.011
2 (2)	92049-01-07-00	53814.482712	1.08 ± 0.02	3.5 ± 0.2	1.47 ± 0.02	1.63 ± 0.14	1.26 ± 0.03
3	93030-01-23-00	54439.248861	1.17 ± 0.03	3.6 ± 0.3	1.52 ± 0.03	1.71 ± 0.08	1.18 ± 0.02
4	93030-01-25-00	54506.856847	1.12 ± 0.03	3.3 ± 0.2	1.38 ± 0.04	1.7 ± 0.2	1.48 ± 0.06
5	94030-01-09-00	54923.374237	0.98 ± 0.02	1.05 ± 0.08	0.668 ± 0.011	1.75 ± 0.03	1.754 ± 0.010
6	94028-01-01-03	54925.797119	1.27 ± 0.03	2.3 ± 0.2	1.03 ± 0.07	1.71 ± 0.05	1.11 ± 0.02
7	94030-01-41-00	55145.515365	1.14 ± 0.03	2.7 ± 0.2	1.28 ± 0.03	1.72 ± 0.11	1.30 ± 0.03
8	95030-01-23-00	55384.878919	1.18 ± 0.03	3.4 ± 0.2	1.52 ± 0.03	1.70 ± 0.05	0.930 ± 0.008
9	95030-01-34-00	55459.229332	1.06 ± 0.03	3.72 ± 0.3	1.45 ± 0.02	1.73 ± 0.03	1.323 ± 0.012
10	96030-01-35-00	55833.989462	1.16 ± 0.03	3.3 ± 0.2	1.36 ± 0.02	1.77 ± 0.07	1.31 ± 0.02
SAX J1808.4–3658							
1	93027-01-01-08	54732.708829	2.23 ± 0.05	2.4 ± 0.2	1.32 ± 0.02	1.70 ± 0.03	1.82 ± 0.02
2	93027-01-01-07	54733.844037	2.27 ± 0.05	2.4 ± 0.2	1.32 ± 0.02	1.64 ± 0.06	2.02 ± 0.02
3	96027-01-01-07	55873.917044	2.68 ± 0.05	2.04 ± 0.13	1.22 ± 0.02	1.52 ± 0.04	2.38 ± 0.03